

## RESEARCH ARTICLE

10.1002/2016TC004244

## Key Points:

- Rock magnetic and macrostructural fabrics identify orogen-parallel midcrustal deformation of the metamorphic core of the Himalayan orogen
- Oblate strain during midcrustal flow may have accommodated oblique convergence without the need for strain partitioning in the upper crust
- Orogen-parallel upper crustal extension followed cessation of midcrustal flow to maintain strain compatibility during oblique convergence

## Supporting Information:

- Supporting Information S1
- Table S1
- Data Set S1
- Data Set S2

## Correspondence to:

A. J. Parsons,  
andrew.parsons@canada.ca

## Citation:

Parsons, A. J., E. C. Ferré, R. D. Law, G. E. Lloyd, R. J. Phillips, and M. P. Searle (2016), Orogen-parallel deformation of the Himalayan midcrust: Insights from structural and magnetic fabric analyses of the Greater Himalayan Sequence, Annapurna-Dhaulagiri Himalaya, central Nepal, *Tectonics*, 35, 2515–2537, doi:10.1002/2016TC004244.

Received 25 MAY 2016

Accepted 11 OCT 2016

Accepted article online 18 OCT 2016

Published online 5 NOV 2016

©2016. The Authors.

This is an open access article under the terms of the Creative Commons Attribution License, which permits use, distribution and reproduction in any medium, provided the original work is properly cited.

# Orogen-parallel deformation of the Himalayan midcrust: Insights from structural and magnetic fabric analyses of the Greater Himalayan Sequence, Annapurna-Dhaulagiri Himalaya, central Nepal

A. J. Parsons<sup>1,2</sup>, E. C. Ferré<sup>3</sup>, R. D. Law<sup>4</sup>, G. E. Lloyd<sup>1</sup>, R. J. Phillips<sup>1</sup>, and M. P. Searle<sup>5</sup>

<sup>1</sup>School of Earth and Environment, University of Leeds, Leeds, UK, <sup>2</sup>Now at Geological Survey of Canada, NRCan, Vancouver, British Columbia, Canada, <sup>3</sup>Department of Geology, Southern Illinois University, Carbondale, Illinois, USA, <sup>4</sup>Department of Geosciences, Virginia Polytechnic Institute and State University, Blacksburg, Virginia, USA, <sup>5</sup>Department of Earth Sciences, University of Oxford, Oxford, UK

**Abstract** The metamorphic core of the Himalaya (Greater Himalayan Sequence, GHS), in the Annapurna-Dhaulagiri region, central Nepal, recorded orogen-parallel stretching during midcrustal evolution. Anisotropy of magnetic susceptibility and field-based structural analyses suggest that midcrustal deformation of the amphibolite facies core of the GHS occurred under an oblate/suboblate strain regime with associated formation of low-angle northward dipping foliation. Magnetic and mineral stretching lineations lying within this foliation from the top of the GHS record right-lateral orogen-parallel stretching. We propose that oblate strain within a midcrustal flow accommodated oblique convergence between India and the arcuate orogenic front without the need for strain partitioning in the upper crust. Oblate flattening may have also promoted orogen-parallel melt migration and development of melt-depleted regions between km<sup>3</sup> scale leucogranite culminations at ~50–100 km intervals along orogen strike. Following the cessation of flow, continued oblique convergence led to upper crustal strain partitioning between orogen-perpendicular convergence on thrust faults and orogen-parallel extension on normal and strike-slip faults. In the Annapurna-Dhaulagiri Himalaya, orogen-parallel stretching lineations are interpreted as a record of transition from midcrustal orogen-perpendicular extrusion to upper crustal orogen-parallel stretching. Our findings suggest that midcrustal flow and upper crustal extension could not be maintained simultaneously and support other studies from across the Himalaya, which propose an orogen-wide transition from midcrustal orogen-perpendicular extrusion to upper crustal orogen-parallel extension during the mid-Miocene. The 3-D nature of oblate strain and orogen-parallel stretching cannot be replicated by 2-D numerical simulations of the Himalayan orogen.

## 1. Introduction

Understanding tectonic evolution of continental-collision zones requires consideration of deformation in three dimensions. Current models of Himalayan orogenesis are largely based on midcrustal kinematic evolution of the orogenic core: the Greater Himalayan Sequence (GHS, Figure 1) [e.g., Searle *et al.*, 2006; He *et al.*, 2014; Montomoli *et al.*, 2015; Cottle *et al.*, 2015; Parsons *et al.*, 2016a, 2016b]. These models describe one of the three generalized end-member processes, (1) channel flow [e.g., Beaumont *et al.*, 2001; Searle *et al.*, 2006], (2) wedge extrusion [e.g., Burchfiel *et al.*, 1992], and (3) underplating/duplexing [e.g., Herman *et al.*, 2010; Montomoli *et al.*, 2015; Carosi *et al.*, 2016], or describe a composite model typically involving channel flow followed by wedge extrusion and/or underplating/duplexing [e.g., Larson *et al.*, 2010; Mukherjee, 2013; Cottle *et al.*, 2015; Parsons *et al.*, 2016a]. Despite their differences, all models consider the kinematic evolution of the GHS in two dimensions and assume (sometimes implicitly) that midcrustal deformation occurred under a plane strain regime. In contrast, present-day and recent upper crustal deformation of the Himalayan orogen is a three-dimensional process, with hinterland orogen-parallel extensional and strike-slip faulting occurring simultaneously to orogen-perpendicular thrust faulting along the frontal thrust system [e.g., Styron *et al.*, 2011].

Anisotropy of magnetic susceptibility (AMS) analysis provides a means to study deformation fabrics, strain kinematics, and strain geometries in three dimensions [e.g., Le Fort, 1981; Rochette *et al.*, 1994;

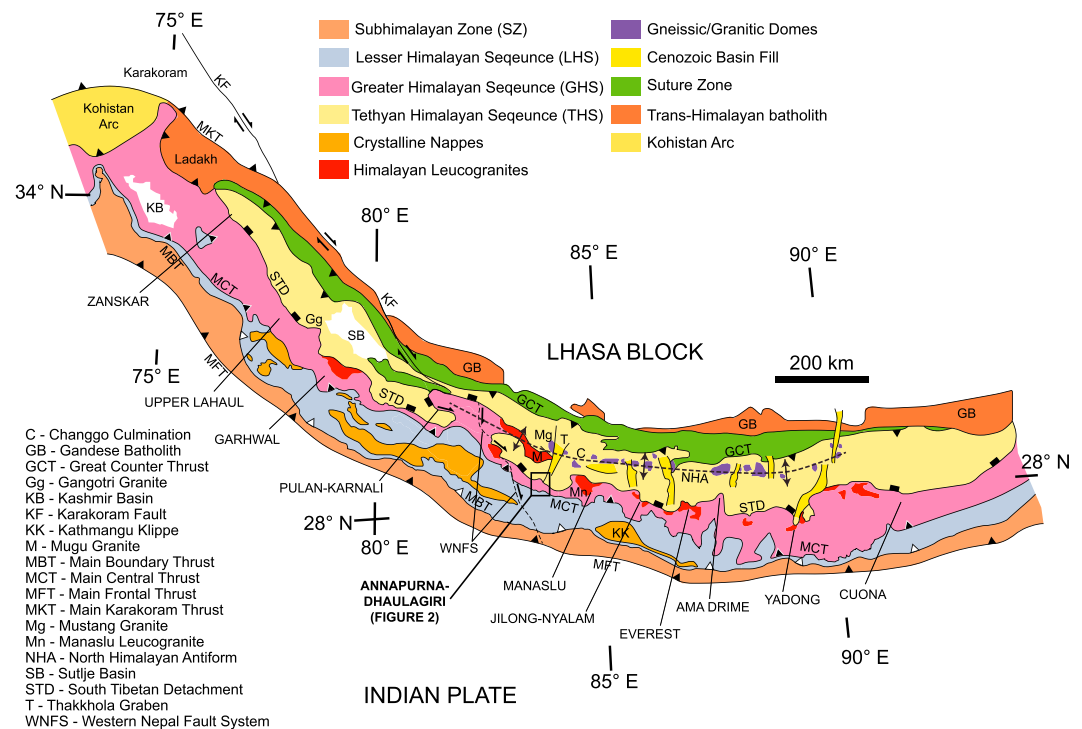


**Figure 1.** Simplified geological map of the Himalayan orogen indicating positions of locations referred to in text [after Goscombe *et al.*, 2006; Searle *et al.*, 2008; Law *et al.*, 2013; Nagy *et al.*, 2015; Silver *et al.*, 2015].

Scaillet *et al.*, 1995; Antolin *et al.*, 2011]. We present rock magnetic fabric and field-based structural data which indicate that the GHS in the Annapurna-Dhaulagiri Himalaya, central Nepal, experienced orogen-parallel stretching and oblate/suboblate strain during midcrustal deformation.

Our data, collected from the GHS and bounding units in the Kali Gandaki Valley (Figure 2), reveal a dominance of orogen-parallel stretching directions lying within low-angle transpositional foliation in the upper portion of the GHS, indicative of an oblique top-down-ENE normal shear sense involving a component of right-lateral orogen-parallel stretching. Additionally, AMS fabric shapes and stretching lineation distributions suggest that the amphibolite facies core of the GHS (the Upper Greater Himalayan Sequence, UGHS) deformed under an oblate/suboblate strain regime during midcrustal flow.

We propose that in the Annapurna-Dhaulagiri Himalaya, oblate strain during midcrustal flow provided a means to maintain strain compatibility during oblique convergence between the Indian and Asian Plates [e.g., Styron *et al.*, 2011]. Oblate strain during crustal flow may have also promoted orogen-parallel melt migration and development of melt-depleted regions, between km<sup>3</sup> scale accumulations of leucogranite such as the neighboring Manaslu and Mugu leucogranite plutons.

Orogen-parallel magnetic and mineral stretching lineations in the GHS are interpreted as an initial record of transition between midcrustal flow and upper crustal orogen-parallel extension. Comparisons with other studies from the Himalaya suggest that an orogen-wide transition from midcrustal orogen-perpendicular flow/extrusion to upper crustal orogen-parallel extension and strike-slip faulting occurred during the mid-Miocene [e.g., Nagy *et al.*, 2015].

## 2. The Annapurna-Dhaulagiri Himalaya

The Himalayan orogeny (Figure 1) initiated during the final closure of Neotethys at ~50 Ma and has maintained convergence since that time [Green *et al.*, 2008; Najman *et al.*, 2010; Searle *et al.*, 2011; Avouac, 2015; Searle, 2015]. In the Annapurna-Dhaulagiri Himalaya (Figure 2), the GHS is bound below and above by the Main Central Thrust (MCT; top-SW) and South Tibetan Detachment (STD; top-down-ENE) and may be

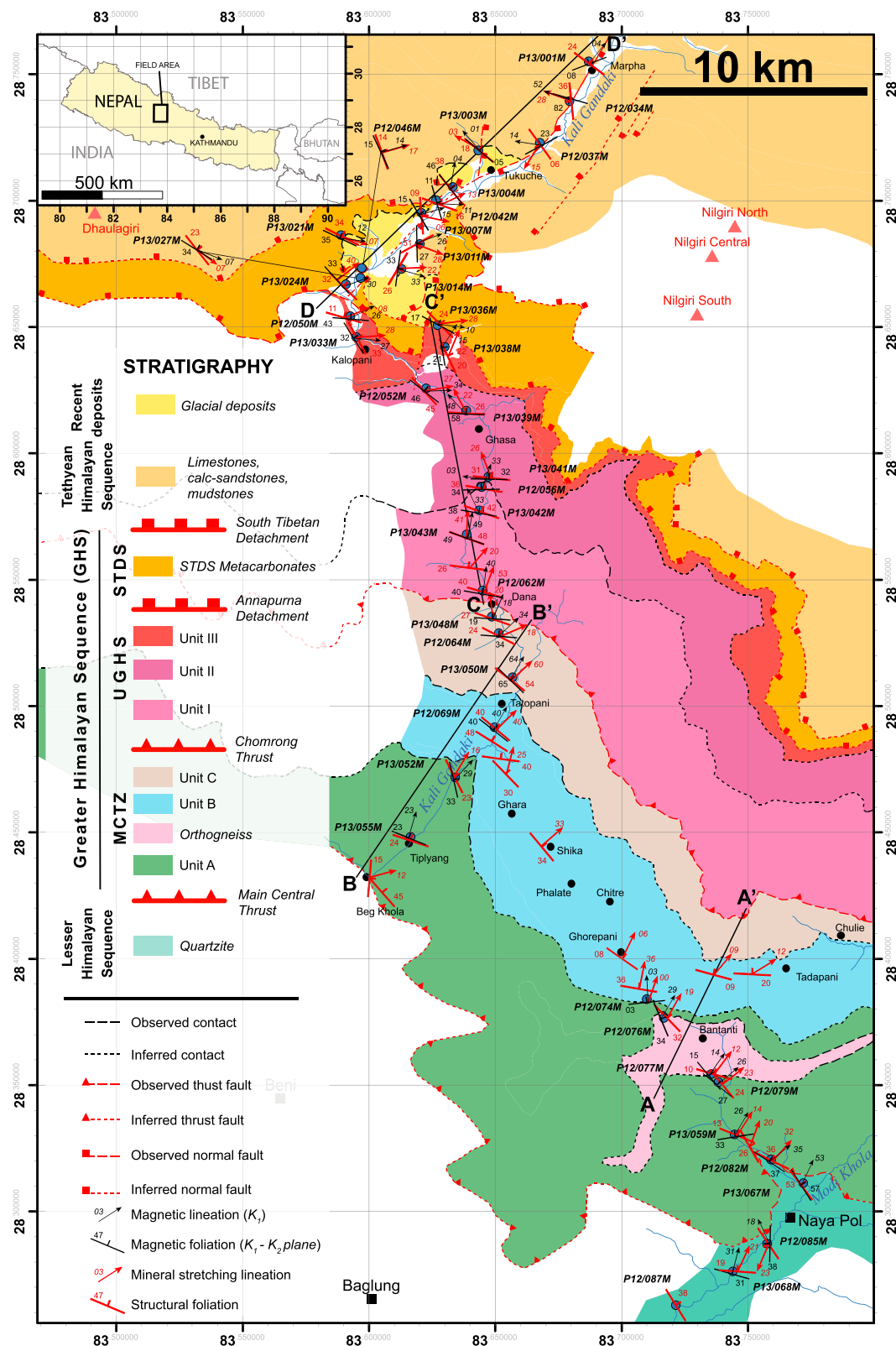


**Figure 2.** Geological map of the Kali Gandaki Valley showing orientations of planar and linear fabrics defined by mineral grain shapes and AMS analyses. Sample locations represented by blue dots, with sample number labels. Lines A-A', B-B', C-C', and D-D' correspond to cross sections in Figure S7.

subdivided into the Main Central Thrust Zone (MCTZ), Upper Greater Himalayan Sequence (UGHS), and South Tibetan Detachment System (STDS) [Larson and Godin, 2009; Carosi et al., 2014; Parsons et al., 2016a, 2016b, 2016c]. Regional-scale tectonic foliation in the GHS (S3) dips ~20–40° NE to ENE, parallel to the bounding shear zones and transposes at least two earlier foliations (S1 and S2) [Godin, 2003; Parsons et al., 2016c]. Mineral stretching lineations associated with S3 are common. For detailed description of regional structure and deformation, see Parsons et al. [2016a, 2016b, and references therein].

The MCTZ was previously defined as the Lower Greater Himalayan Sequence (LGHS) [Parsons et al., 2016c]. Recent work from Parsons et al. [2016a] demonstrated that the structural evolution of this section of the GHS reflects that of a crustal-scale top-SW shear zone, synonymous to the Main Central Thrust Zone (MCTZ) as described by Bouchez and Pêcher [1981], Grasemann et al. [1999], Mottram et al. [2015], Larson et al. [2015], and others. Based on these studies, the LGHS of Parsons et al. [2016c] is more appropriately defined as the MCTZ.

## 2.1. Tectonostratigraphy

The Lesser Himalayan Sequence (LHS) underlies the GHS and contains chlorite and lower grade quartzites and metapelites. Deformation temperature estimates range between <280°C and 300–400°C [Parsons et al., 2016a].

At the base of the GHS, the MCTZ overlies the LHS and contains lower to upper greenschist facies metasedimentary rocks, which divide upsection (Figure 2) into Unit A—metapelites, metasediments, quartzites, and orthogneiss; Unit B—quartzites and marbles; and Unit C—dolomitic marbles and metapelites. The Chomrong Thrust (CT; top-SW) bounds the top of the MCTZ. The MCTZ recorded pervasive top-SW noncoaxial plane strain deformation at temperatures of ~300°C to 550–650°C [Parsons et al., 2016a]. Peak metamorphism is constrained between ~500–650°C and ~7–12 kbar [Le Fort et al., 1987; Vannay and Hodges, 1996].

Above the MCTZ, the UGHS contains amphibolite facies paragneisses and orthogneisses, schists, and migmatites, with leucosomes and leucogranite intrusions throughout. The UGHS divides (Figure 2) into Unit I—psammitic and pelitic paragneiss, schists, and migmatites; Unit II—calc-silicate gneiss and migmatites; and Unit III—orthogneiss, migmatites, and subordinate calc-silicate gneiss. The UGHS is capped by the Annapurna Detachment (AD; top-down-ENE). The UGHS recorded pervasive general shear with components of oblate and coaxial plane strain at temperatures of 550–800°C [Larson and Godin, 2009; Parsons et al., 2016a, 2016b]. Shear sense indicators record top-SW motion in Unit I and top-down-ENE in Unit III. Synmigmatitic deformation is observed at outcrop and microstructural scale [Larson and Godin, 2009; Parsons et al., 2016a, 2016b]. Metamorphic mineral equilibration occurred within the kyanite stability field [Carosi et al., 2015], with peak metamorphism between ~650–800°C and ~10–12 kbar [Iaccarino et al., 2015; Parsons et al., 2016b]. Prograde metamorphism initiated at ~48–43 Ma, followed by partial melting between 41 and 18 Ma [Larson and Cottle, 2015; Carosi et al., 2015; Iaccarino et al., 2015]. Retrograde metamorphism occurred at ~41–30 Ma and ~25–18 Ma, in Unit III and Unit I, respectively [Iaccarino et al., 2015; Carosi et al., 2016]. U-Pb geochronology of undeformed leucogranite suggests that motion on the CT occurred before 18.5–22 Ma [Nazarchuk, 1993; Hodges et al., 1996].

At the top of the GHS, the STDS forms a pervasive ductile shear zone containing carbonate metasedimentary rocks, subordinate calc-silicate gneisses, and leucogranites. Top-down-ENE noncoaxial shearing is observed throughout the shear zone [Parsons et al., 2016a, 2016b]. Poorly constrained deformation temperature estimates range between >700°C and 300–600°C [Parsons et al., 2016a]. Peak metamorphism occurred at  $730 \pm 60^\circ\text{C}$  [Parsons et al., 2016b]. U-Pb geochronology of deformed and undeformed leucogranites suggests that motion on the AD ceased by ~22 Ma [Godin et al., 2001].

The Tethyan Himalayan Sequence (THS) overlies the GHS and contains chlorite to lower grade calcareous and pelitic metasedimentary rocks. At its base STDS-parallel transpositional foliation (S3) overprints earlier fold-and-thrust-related deformation [Godin, 2003; Parsons et al., 2016b, 2016c]. Deformation temperature estimates range between <300 and 400°C [Parsons et al., 2016a]. In the upper Kali Gandaki Valley, E-W extension on the Thakkhola graben deformed the THS between mid-Miocene to Plio-Pleistocene times, via normal faulting along the NNE-SSW striking Dangardzong fault [Hurtado et al., 2001; Hurtado, 2002; Garzone et al., 2003]. STDS-parallel low-angle normal faulting possibly continued into the Pleistocene (Dhaulagiri Detachment) [McDermott et al., 2015].

### 3. Anisotropy of Magnetic Susceptibility (AMS)

Magnetic susceptibility ( $K$ ) is defined as the ratio between magnitudes of an externally applied magnetic field ( $H$ ) and an object's corresponding induced magnetization ( $M$ ).

$$M = K H \quad (1)$$

Anisotropy of magnetic susceptibility (AMS) describes directional variation of an object's magnetic susceptibility ( $K$ ) as a second rank tensor. In geological materials, AMS is controlled by mineral content, mineral shape fabric, and crystallographic fabric [Borradaile and Jackson, 2004]. AMS can be used to investigate deformation kinematics if contributions of controlling factors are determined [Borradaile and Jackson, 2010]. The AMS ellipsoid is defined by three mutually orthogonal principal susceptibility axes,  $K_1$  (maximum),  $K_2$  (intermediate), and  $K_3$  (minimum) [Tarling and Hrouda, 1993].  $K_1$  is commonly referred to as the magnetic lineation.  $K_3$  represents the pole to magnetic foliation ( $K_1$ - $K_2$  plane). Bulk susceptibility ( $K_m$ ) is the mean of  $K_1$ ,  $K_2$ , and  $K_3$  [Janák, 1965].

The *corrected degree of anisotropy* ( $P'$ —magnetic anisotropy from hereafter) describes strength of AMS in terms of deviation from a sphere ( $P' = 1$ ) to an ellipsoid ( $P' > 1$ ) [Jelinek, 1981].

$$P' = \exp \sqrt{2 \sum (\ln K_i - \ln K_m)^2} \quad (2)$$

$K_i$  refers to the three susceptibility axes,  $K_1$ ,  $K_2$ , and  $K_3$ . The shape parameter  $T$  ( $-1 \leq T \leq 1$ ) describes magnetic susceptibility ellipsoid shape in terms of prolate ( $T = -1$ ;  $K_1 > K_2 = K_3$ ) and oblate ( $T = 1$ ;  $K_1 = K_2 > K_3$ ) end-members [Jelinek, 1981].

$$T = \frac{\ln(F) - \ln(L)}{\ln(F) + \ln(L)} \quad \text{where} \quad L = \frac{K_1}{K_2} \quad \text{and} \quad F = \frac{K_2}{K_3} \quad (3)$$

#### 3.1. Controlling Factors of AMS

In order to make meaningful interpretations from AMS data, factors controlling the AMS of individual samples must be determined [e.g., Wallis et al., 2014a]. Potential controlling factors are briefly outlined below and reviewed in detail by Tarling and Hrouda [1993], Tauxe [2002], and Borradaile and Jackson [2004, 2010].

Magnetic materials may be classed as *diamagnetic*, *paramagnetic*, or *ferromagnetic*, listed in order of strength of induced magnetization [Tarling and Hrouda, 1993; Tauxe, 2002]. Induced magnetization of diamagnetic materials is diametrically opposed to the external field (–ve  $K$ ). Induced magnetization of paramagnetic and ferromagnetic (sensu lato) materials occurs in the same direction as the external field (+ve  $K$ ). Diamagnetic (e.g., quartz and calcite) and paramagnetic (e.g., phyllosilicate) materials lose induced magnetization instantaneously upon removal of the external field. Most ferromagnetic minerals possess strong (e.g., magnetite) or weak (e.g., hematite) remanent magnetism [Tarling and Hrouda, 1993].

Grain-scale AMS is affected by grain shape (magnetostatic anisotropy) and crystal structure (magnetocrystalline anisotropy), whereby AMS axes align parallel or orthogonal to grain shape or crystal axes. Magnetization of ferromagnetic minerals is affected by grain size, which determines the number of magnetic domains (regions of uniform magnetism with a single dipole) within a grain [Tauxe, 2002]. For magnetite, grain size from smallest to largest is classified as *single domain* (SD, typically  $< 0.1 \mu\text{m}$ ), *pseudo single domain* (PSD), and *multiple domain* (MD). Very small SD grains ( $\leq 0.05 \mu\text{m}$ ), which lose their remanent magnetism almost instantaneously, are *superparamagnetic* (SP) [Tarling and Hrouda, 1993; Tauxe, 2002].

Whole-rock AMS fabrics reflect summation of grain-scale anisotropies of all constituent grains, plus effects of grain shape preferred orientation (SPO) and crystallographic preferred orientation (CPO). AMS fabrics are controlled by the magnetically predominant mineral phase(s), referred to as magnetic carrier(s) [Borradaile and Jackson, 2004]. Strong SPO of ferrimagnetic minerals and CPO of all other minerals may produce a magnetic lineation and/or foliation that mimics mineral fabrics [Borradaile, 1991; Borradaile and Jackson, 2010]. AMS fabrics may be influenced by magnetostatic interactions between ferromagnetic grains. Significance of such interactions depends on the spatial distribution and concentration of ferromagnetic grains [Hargraves et al., 1991; Stephenson, 1994; Muxworthy et al., 2004].



**Table 1.** AMS Results<sup>a</sup>

Sample	Structural Height Relative to MCT (m)	Lithology	Tectonic Unit	Number of Cubes, <i>n</i>	Mean $K_m$ ( $\times 10^{-6}$ )	Mean $P'$	Mean $T$	$K_1$ Mean Orientation	$K_2$ Mean Orientation	$K_3$ Mean Orientation
P13/001M	17330	Marl/Micaceous Limestone	THS	16	88.83	1.054	−0.854	82/159	07/308	04/039
P12/034M	17175	Marl/Micaceous Limestone	THS	9	4.01	1.535	0.225	09/106	79/251	07/015
P12/037M	16500	Marl/Micaceous Limestone	THS	15	277.09	1.118	−0.085	14/279	18/013	67/153
P13/003M	15675	Dolomitic Quartzite	THS	16	29.14	1.037	0.034	85/220	05/049	01/319
P13/004M	14930	Metacarbonate	THS	15	90.20	1.113	0.106	44/030	11/131	44/232
P12/042M	14750	Metacarbonate	STDS	15	969.60	3.184	0.149	11/092	04/001	79/254
P13/007M	14450	Porphyritic Biotite-metacarbonate	STDS	14	102.38	1.043	0.483	15/073	03/342	75/239
P13/011M	14025	Marble	THS	11	20.85	1.080	−0.396	26/070	07/164	63/269
P13/021M	13500	Calc-sandstone/metacarbonate	STDS	14	26.31	1.112	0.549	12/097	33/359	55/205
P13/014M	13475	Marble	THS	21	179.86	1.231	0.004	33/106	04/014	57/278
P12/046M	13125	Marble	STDS	14	339.07	1.578	0.279	14/076	04/345	75/240
P13/027M	13050	Calc-silicate gneiss	STDS	14	609.09	2.108	0.230	07/111	33/016	56/212
P13/024M	12700	Calc-silicate migmatite	STDS	19	99.67	1.211	0.902	30/070	11/336	57/225
P13/036M	12630	Marble	STDS	15	545.75	1.618	0.283	10/097	24/002	63/208
P12/050M	12400	Orthogneiss	Unit III, UGHS	16	57.95	1.253	0.880	10/084	41/345	47/185
P13/038M	12230	Calc-silicate migmatite	Unit III, UGHS	15	203.23	1.297	0.785	15/033	15/127	69/260
P13/033M	12200	Leucogranite	Unit III, UGHS	23	40.92	1.206	0.914	27/095	17/356	58/238
P12/052M	11300	Calc-silicate gneiss	Unit II, UGHS	16	117.19	1.017	0.098	44/218	34/087	27/337
P13/039M	11000	Calc-silicate migmatite	Unit II, UGHS	15	455.25	1.481	0.782	48/317	24/077	32/183
P13/041M	9525	Calc-silicate migmatite	Unit II, UGHS	15	88.20	1.134	0.777	03/276	32/008	58/181
P12/056M	9175	Pelitic migmatite	Unit I, UGHS	16	1955.63	1.953	0.690	33/020	10/283	56/179
P13/042M	8650	Pelitic migmatite	Unit I, UGHS	17	3639.41	2.434	0.916	33/335	18/077	52/190
P13/043M	7775	Pelitic migmatite	Unit I, UGHS	16	81.44	1.107	0.762	49/010	05/105	41/200
P12/062M	6300	Quartzite	Unit I, UGHS	19	220.05	1.897	0.714	40/007	02/098	50/190
P13/048M	5650	Metacarbonate	MCTZ	13	66.91	1.047	−0.333	71/184	06/292	18/023
P12/064M	5450	Calc-phyllite	MCTZ	15	947.47	1.905	0.218	34/046	04/139	56/235
P13/050M	4725	Calc-phyllite	MCTZ	14	909.93	3.430	0.035	64/031	05/131	25/224
P12/069M	3300	Quartzite	MCTZ	12	6.49	1.918	0.681	40/030	04/124	50/219
P12/074M	3200	Quartzite	MCTZ	14	11.92	1.862	0.850	03/354	00/084	87/175
P12/076M	2725	Augen orthogneiss	MCTZ	15	91.65	1.107	0.337	28/033	14/131	58/245
P13/052M	2025	Semipelite	MCTZ	13	44.27	1.215	0.745	29/043	16/141	57/257
P12/077M	1600	Augen orthogneiss	MCTZ	14	49.89	1.131	0.269	14/034	04/125	75/230
P12/079M	1225	Quartzite	MCTZ	15	54.18	1.076	0.048	26/051	05/319	64/220
P13/055M	875	Semipelite	MCTZ	15	120.84	1.376	0.924	23/016	01/106	67/198
P13/059M	300	Semipelite	MCTZ	20	41.01	1.205	0.721	26/031	18/292	57/171
P12/082M	0	Quartzite	MCTZ	14	34.73	1.386	0.812	35/052	09/315	54/213
P12/085M	−150	Quartzite	LHS	18	80.83	1.203	0.465	17/337	32/236	53/090
P13/067M	−425	Quartzite	LHS	17	3.70	1.328	0.284	53/025	16/137	33/238
P13/068M	−900	Quartzite	LHS	13	10.88	1.447	0.543	31/014	01/104	59/196
P12/087M	−2400	Quartzite	LHS	16	8.10	1.082	−0.032	21/053	63/275	17/150

<sup>a</sup>Samples listed in order of vertical structural height above the MCT. Mean magnetic properties of each sample and the orientation of the resulting magnetic fabrics and magnetic lineations, plus the locally measured structural foliation and mineral lineation orientations. Magnetic carrier of each sample is also given.  $K_m$ , bulk susceptibility;  $P'$ , corrected degree of anisotropy;  $T$ , shape parameter—see the supporting information Data Set S1 for full AMS data set. See supporting information Table S1 for detailed summary of all magnetic carriers.

AMS fabrics controlled by SPO and/or CPO fabrics may correlate with 3-D strain, such that principal susceptibility axes ( $K_1 \geq K_2 \geq K_3$ ) and finite strain axes ( $X \geq Y \geq Z$ ) are parallel [Borradaile, 1991; Borradaile and Jackson, 2010; Kruckenberg et al., 2010, 2011; Ferré et al., 2014, 2016]. Correlations may also exist between  $P'$  and finite strain magnitude [e.g., Benn, 1994; Tripathy, 2009] and between  $T$  and strain geometry [e.g., Sidman et al., 2005]. Magnetic carriers must be determined, and competing factors that control/influence AMS must be investigated before such correlations can be made [Borradaile and Jackson, 2010; Ferré et al., 2014; Wallis et al., 2014a].

### 3.2. Analytical Methods

Magnetic fabric analyses were conducted at the Department of Geology, Southern Illinois University, following procedures recommended by Ferré et al. [2003, 2004] and Kruckenberg et al. [2010]. Forty field-orientated samples were analyzed from the Kali Gandaki Valley and surrounding foothills (Figure 2 and Table 1). Cubes (17–18 mm) cut from each sample (614 cubes) were analyzed using an AGICO KLY-4S Kappabridge susceptometer at 300 A/m [Pokorný et al., 2004]. A minority of samples with low susceptibility were analyzed at 450 A/m. AMS data were acquired using SUFAR 1.2 and processed with Anisoft 4.2 to

**Table 1.** (continued)

Local Structural Foliation/Bedding	Local Structural Lineation	Magnetic Foliation	Magnetic Lineation	Magnetic Material Type	Dominant Carrier of Magnetic Susceptibility	Longitude	Latitude
127/24°NE	-	069/08°NW	04/039	Paramagnetic	Phyllosilicate	83.6868668	28.75452183
174/36°W	28/289	106/82°SW	52/288	Diamagnetic	Quartz and/or calcite	83.6794804	28.74004017
144/06°S	15/211	062/23°N	14/279	Ferromagnetic	Pyrrhotite	83.6681007	28.7221676
129/18°NE	03/295	130/05°NE	01/319	Paramagnetic	Muscovite	83.6438134	28.71782393
142/38°NE	-	142/46°NE	04/010	Ferromagnetic	SD pyrrhotite	83.63271752	28.70487297
110/16°N	13/076	164/11°E	11/092	Ferromagnetic	Pyrrhotite and/or SD-MD/PSD magnetite	83.6262988	28.69993788
166/09°NE	06/101	149/15°NE	15/073	Paramagnetic	Phyllosilicate	83.620635	28.694594
061/51°SE	28/110	179/27°E	26/070	Ferromagnetic	SD pyrrhotite	83.6199189	28.68310316
118/34°N	07/107	115/35°N	12/097	Paramagnetic	Phyllosilicate	83.5889272	28.68603288
030/26°SE	22/087	008/33°E	33/106	Ferromagnetic	MSD magnetite or SD pyrrhotite	83.6122165	28.67285092
165/14°E	17/073	155/15°E	14/073	Ferromagnetic	Pyrrhotite-SD-MD magnetite mix	83.5972995	28.67225966
143/23°NE	07/120	122/34°NE	07/111	Ferromagnetic	Pyrrhotite ± SD-MD magnetite	83.5965577	28.67096055
134/32°NE	40/052	135/33°NE	30/070	Ferromagnetic	SD-SP magnetite and/or pyrrhotite	83.59037584	28.66704360
126/24°NE	28/082	118/17°N	10/097	Ferromagnetic	Pyrrhotite-SD-MD-SP/PSD magnetite mix	83.6266725	28.65039706
112/11°N	08/069	095/43°N	26/064	Paramagnetic	Phyllosilicate	83.5932506	28.65373892
143/20°NE	22/022	170/21°E	15/033	Ferromagnetic	Pyrrhotite and/or SD-MD magnetite	83.630059	28.64170645
148/33°NE	28/085	148/32°NE	27/095	Paramagnetic	Phyllosilicate	83.59475404	28.64640786
138/45°N	27/079	128/46°NE	34/087	Paramagnetic	Diopside and/or phlogopite	83.6224836	28.62549568
096/26°N	22/331	093/58°N	48/317	Ferromagnetic	SD-MD/PSD magnetite	83.63825871	28.61593486
096/31°N	26/338	091/32°N	03/276	Paramagnetic	Biotite and/or diopside	83.6479879	28.59030124
098/36°E	-	089/34°N	33/019	Ferromagnetic	SD-MD/PSD magnetite ± minor SP magnetite	83.6450305	28.58614273
110/42°N	-	100/38°N	33/335	Ferromagnetic	MD (Ti-) magnetite ± SD (Ti-)magnetite	83.64402463	28.57709438
110/48°N	41/003	110/49°N	49/010	Paramagnetic	Phyllosilicate	83.639318	28.56712092
106/40°N	53/010	100/40°N	40/007	Ferromagnetic	SD-MD magnetite ± minor SP magnetite	83.6453387	28.54509462
109/27°N	20/352	094/19°N	18/023	Paramagnetic	Phyllosilicate	83.65177051	28.52812420
117/24°N	18/067	106/ 34°N	34/047	Ferromagnetic	Pyrrhotite-SD-MD magnetite mix	83.6517705	28.5281242
128/54°NE	60/046	134/65°NE	64/031	Ferromagnetic	SD-MD magnetite ± Pyrrhotite	83.65662103	28.51106745
134/40°N	40/043	128/40°N	40/031	Paramagnetic	Phyllosilicate	83.6498073	28.49130309
172/00	00/019	084/03°N	03/357	Paramagnetic	Phyllosilicate	83.711069	28.38403962
135/32°N	19/024	157/34°N	29/031	Paramagnetic	Phyllosilicate	83.7173726	28.37695666
158/23°NE	16/030	167/33°NE	29/043	Paramagnetic	Phyllosilicate	83.633737	28.471542
118/10°N	12/036	140/15°N	14/034	Paramagnetic	Phyllosilicate	83.7361496	28.3544546
140/24°N	23/052	129/27°N	26/050	Paramagnetic	Phyllosilicate	83.7393014	28.35091312
102/24°N	-	108/23°N	23/016	Paramagnetic	Phyllosilicate	83.6167908	28.44751686
112/13°N	14/033	081/33°N	26/031	Paramagnetic	Phyllosilicate	83.74481701	28.33036635
114/36°N	32/042	123/37°N	35/051	Paramagnetic	Phyllosilicate	83.7588184	28.32030681
156/45°W	23/202	001/38°W	18/336	Paramagnetic	Chlorite	83.7586966	28.28786063
143/53°NE	-	148/57°NE	53/025	Diamagnetic	Quartz	83.77168537	28.31084507
094/19°N	21/024	106/31°N	31/014	Paramagnetic	Phyllosilicate	83.74486336	28.27654758
148/38°W	-	-	48/045	Diamagnetic	Quartz	83.7220948	28.26262096

determine mean magnitudes and orientations of principal susceptibility axes [Chadima and Jelinek, 2008], based on directional statistics of Jelinek [1978, 1981].

Magnetic hysteresis analyses were conducted on one to three cubes from each sample to determine magnetic carrier types [e.g., Dunlop, 2002a]. First-Order Reversal Curve (FORC) analyses were conducted on samples with ferromagnetic carriers to measure magnetostatic grain interactions [e.g., Muxworthy et al., 2004]. These analyses were conducted with a Princeton 3900-04 vibrating sample magnetometer up to a field of  $7.94 \times 10^5$  A/m (1 T). FORC data were processed using FORCinel 1.21 [Harrison and Feinberg, 2008]. Scanning electron microscopy (SEM), electron dispersive spectroscopy (EDS), and electron backscatter diffraction (EBSD) analyses aided identification of magnetic carriers (Text S1 and Figures S3 and S4 in the supporting information).

## 4. Results

### 4.1. AMS Parameters ( $K_m$ , $P'$ , and $T$ )

The full AMS data set is presented in Data Set S1. Sample mean bulk susceptibility ( $K_m$ ) varies between  $3.70 \times 10^{-6}$  and  $3639.41 \times 10^{-6}$  (SI) (Table 1), reflecting variety of diamagnetic, paramagnetic, and

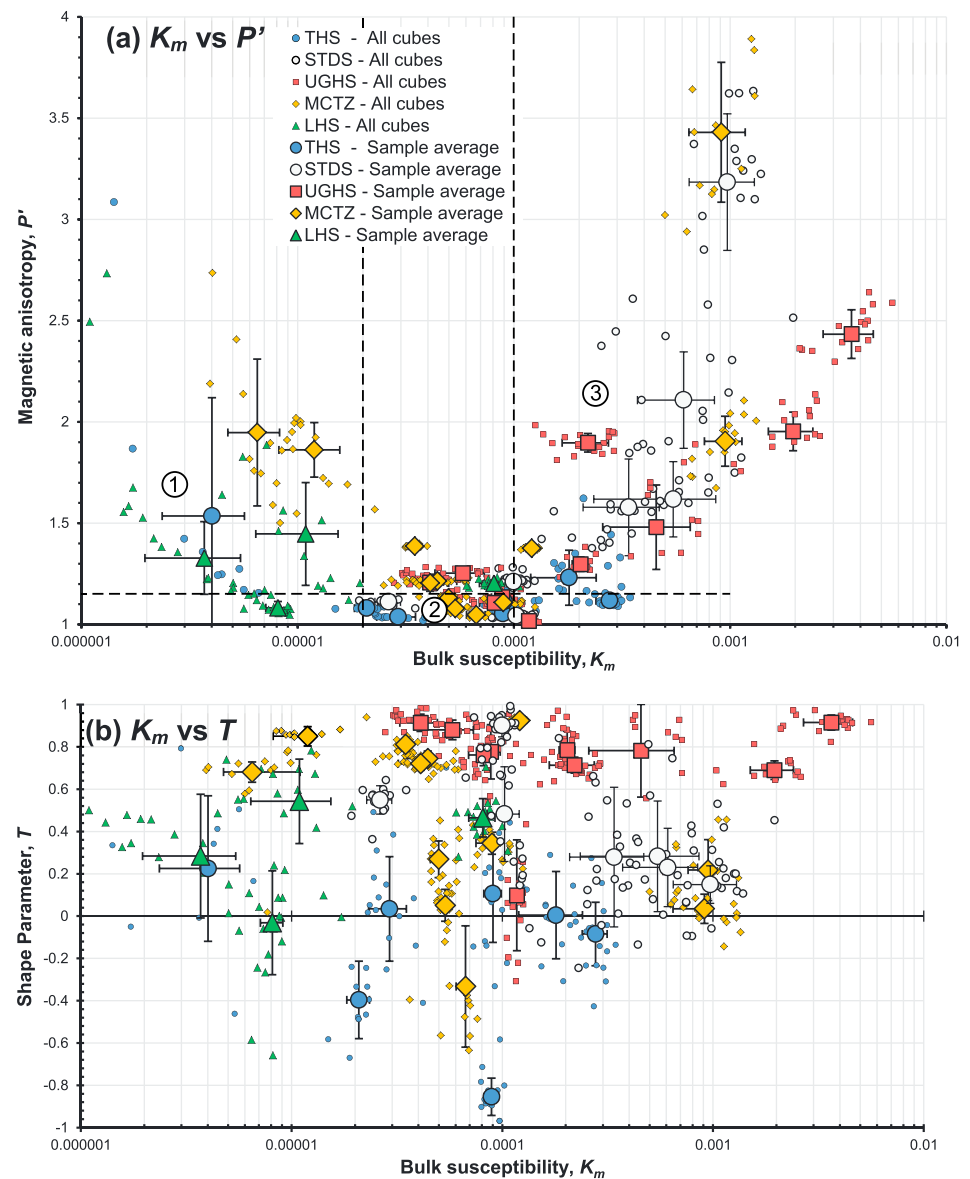


**Figure 3.** AMS results. (a) Magnetic anisotropy ( $P'$ ) versus bulk susceptibility ( $K_m$ ). Dashed lines delineate typical  $K_m$ - $P'$  values for, (1) diamagnetic, (2) paramagnetic phyllosilicates, and (3) ferromagnetic minerals. (b) Shape parameter ( $T$ ) versus bulk susceptibility ( $K_m$ ). Error bars = 1 standard deviation.

ferromagnetic carriers (Figure 3). Mean  $P'$  varies between 1.01 and 3.43 and does not correlate with tectonostratigraphy (Figure 3a and Table 1).

The maximum magnetic anisotropy ( $P'$ ) that can be obtained from well-oriented paramagnetic silicates reflects the intrinsic magnetic anisotropy of such minerals ( $P' \leq 1.36$ ) and could only be attained by a monomineralic assemblage of perfectly oriented grains [Martín-Hernández and Hirt, 2003]. As this is not the case, maximum magnetic anisotropy attributed to paramagnetic silicates in schists and mylonites culminates typically at  $P' \approx 1.15$  [Martín-Hernández and Ferré, 2007].  $P' > 1.15$  is likely to arise from ferromagnetic (sensu lato) contributions to AMS. Figure 3a provides valuable information on the origin of AMS in our samples. Samples with  $K_m < 20 \times 10^{-6}$  (SI) and  $P' > 1.15$  display AMS typically dominated by diamagnetic and, to a minor extent, other minerals. These samples display negative correlation between  $K_m$  and  $P'$ ; however, these values are too close to the sensitivity of the Kappabridge instrument to be interpreted with confidence. Samples with  $20 \times 10^{-6}$  (SI)  $< K_m < 100 \times 10^{-6}$  (SI) and  $P' < 1.15$  are characteristic of paramagnetic fabrics



dominated by magnetocrystalline phyllosilicates. There is no correlation between  $P'$  and  $K_m$  between these ranges, most likely because the maximum fabric strength is bound by the intrinsic magnetic anisotropy. Samples with  $K_m > 100 \times 10^{-6}$  (SI) and  $P' > 1.15$  display AMS dominated by magnetostatic anisotropy of ferromagnetic (sensu lato) carriers such as magnetite or pyrrhotite. Correlation between  $P'$  and  $K_m$  at this range is typical of such ferromagnetic phases [e.g., Ferré *et al.*, 1997].

Mean  $T$  ranges between  $-0.85$  (prolate) and  $0.92$  (oblate) (Figure 3b).  $T$  correlates roughly with tectonostratigraphy, with mean  $T$  of  $-0.06$  for the THS,  $0.41$  for the STDS,  $0.73$  for the UGHS,  $0.44$  for the MCTZ, and  $0.32$  for the LHS.  $T$  is dominantly oblate for most samples in the UGHS, while samples from the STDS produce suboblate fabrics (Figure 3b). In the MCTZ, specimens dominated by paramagnetic minerals have oblate ellipsoids, whereas specimens dominated by ferromagnetic carriers display more triaxial ellipsoids.

Mean principal axis orientations for  $K_1$ ,  $K_2$ , and  $K_3$  are presented in Table 1.  $K_1$  plunge and azimuth typically ranges between  $10$  and  $50^\circ$  northwest to east.  $K_3$  typical plunges  $40$ – $80^\circ$  toward west to south.

#### 4.2. Magnetic Carriers

To constrain the origin of AMS (i.e., magnetic carrier(s)), we supplement AMS analyses with magnetic hysteresis and FORC analyses (Figures S1 and S2) to assess the abundance of magnetic mineral species and determine which phases are present and likely to contribute to AMS. Only complete, well-defined hysteresis loops are used in interpretation of magnetic carriers (Figure S1 and Table S1). Contributions of specific phases to AMS are further evaluated through EBSD-CPO analysis of paramagnetic phases (i.e., phyllosilicates) (Figure S3) and electron microscopy and EDS of minor ferromagnetic phases (i.e., pyrrhotite and magnetite) (Figure S4). Hysteresis and FORC diagrams (Data Set S2) are included in Figures S1 and S2.

A range of magnetic responses indicative of diamagnetic, paramagnetic, and ferromagnetic (sensu lato) carriers were recorded. In general, results produced by multiple specimen cubes of the same sample were consistent, suggesting homogenous ferromagnetic phase and grain size distributions. A few samples produced nonself-consistent results that may reflect uneven ferromagnetic phase and grain size distributions across the sample. Identified magnetic carriers are listed in Tables 1 and S1.

Mineral assemblages of all three diamagnetic samples in the LHS and THS (P12/034M, P12/087M, and P13/067M) indicate that quartz ( $\pm$ calcite) SPO/CPO must define their AMS (Table 1).

Microscopy of mineral assemblages indicates that phyllosilicates form magnetic carriers in 21 paramagnetic samples from the LHS, GHS, and THS (Table 1). Correlation between paramagnetic AMS fabric orientations and EBSD-derived phyllosilicate CPOs suggests that phyllosilicate CPO controls the AMS of most of these samples (Figure S3). Diopside and/or phyllosilicate CPO/SPO form magnetic carriers in P12/052M and P13/041M (calc-silicate gneisses, UGHS—Table 1). Paramagnetic slope correction of hysteresis loops typically reveals minor volumes ( $<0.1\%$ ) of ferromagnetic phases within paramagnetic and diamagnetic samples (Figure S1 and Table S1).

Dominant carriers of magnetic susceptibility in 16 ferromagnetic samples were determined through comparison of hysteresis loop and FORC diagram geometries and parameters with previously published data sets [e.g., Tauxe *et al.*, 1996; Pike *et al.*, 1999; Roberts *et al.*, 2000, 2006; Dunlop, 2002a, 2002b; Tauxe, 2002; Muxworthy *et al.*, 2004]. In these samples, magnetic carriers are identified as magnetite, pyrrhotite, or a mix of both phases (Table 1). SEM/EDS analysis confirms the presence of these phases as interstitial grains and inclusions (Table S1 and Figure S4). Pyrrhotite and/or SD magnetite probably form dominant carriers in samples with high squareness ratios ( $M_R/M_S \geq 0.5$ ;  $M_S$ , magnetic saturation;  $M_R$ , magnetic remanence) and low field saturation ( $H_S \leq 600$  kA/m; e.g., P12/037M, P13/004M, P13/021M, and P13/038M—Table S1) [Dunlop, 2002a, 2002b; Tauxe, 2002; Roberts *et al.*, 2006]. Samples with  $M_R/M_S \leq 0.2$  and  $H_{CR}/H_C > 2.0$  ( $H_C$ , coercivity;  $H_{CR}$ , coercivity of remanence) are characteristic of MD  $\pm$  SD magnetite (e.g., P12/056M, P12/062M, and P13/042M—Table S1) [Dunlop, 2002a, 2002b; Tauxe, 2002]. Many hysteresis loops display “wasp-waist” and “pot-bellied” defects [Tauxe *et al.*, 1996; Tauxe, 2002], suggesting a mix of ferromagnetic phases and/or grain sizes (e.g., P12/046M, P12/064M, P13/024M, P13/027M, and P13/050M—Figure S1). FORC diagrams are comparable to previously published SD and MD magnetite data (peak  $H_C < 20$  mT; e.g., P12/042M, P12/046M, P12/056M, P13/027M, P13/038M, P13/039M, and P13/042M—Figure S2) and pyrrhotite data (peak  $H_C = 20$ – $60$  mT; e.g., P12/037M, P13/004M, and P13/011M—Figure S2) [Pike *et al.*, 1999;

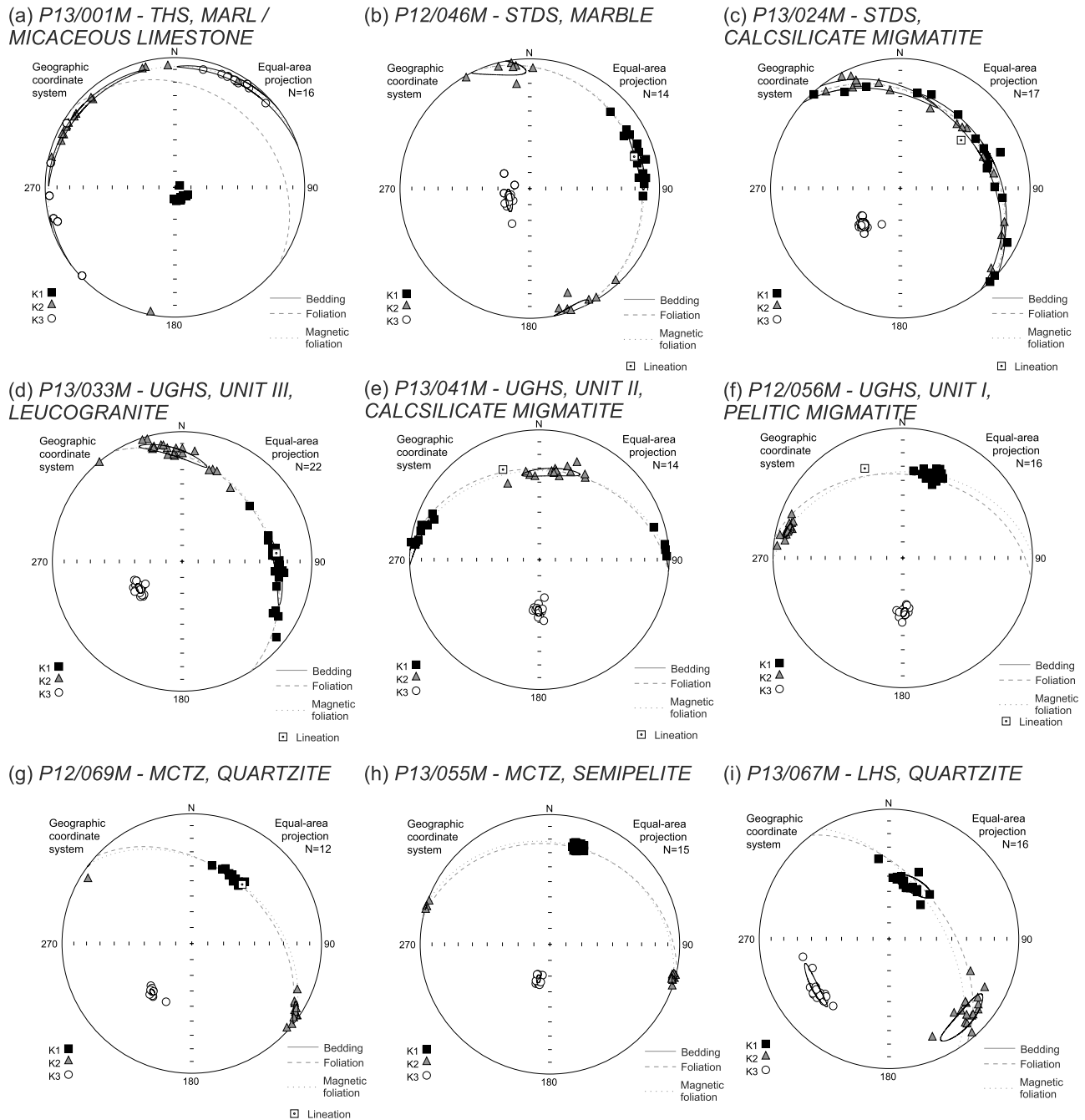


**Figure 4.** Stereographic projections of selected AMS data sets from individual hand samples. Stereonets show principal susceptibility axis orientations,  $K_1$ ,  $K_2$ , and  $K_3$  for all cubes of a single sample. The 95% confidence ellipses are also shown.  $N$  = number of cube specimens per sample.

Roberts *et al.*, 2000, 2006; Muxworthy *et al.*, 2004]. FORC analyses indicate that magnetostatic interaction between grains is negligible, indicated by only minor vertical spreading of contours from density maxima (Figure S2).

## 5. Correlation Between AMS Fabrics and Deformation in the Annapurna-Dhaulagiri Himalaya

The magnetic carrier(s) of every sample cannot be identified with absolute certainty; however, consistent trends in AMS ellipsoid orientation and shape, and strong correlation between macrostructural and magnetic

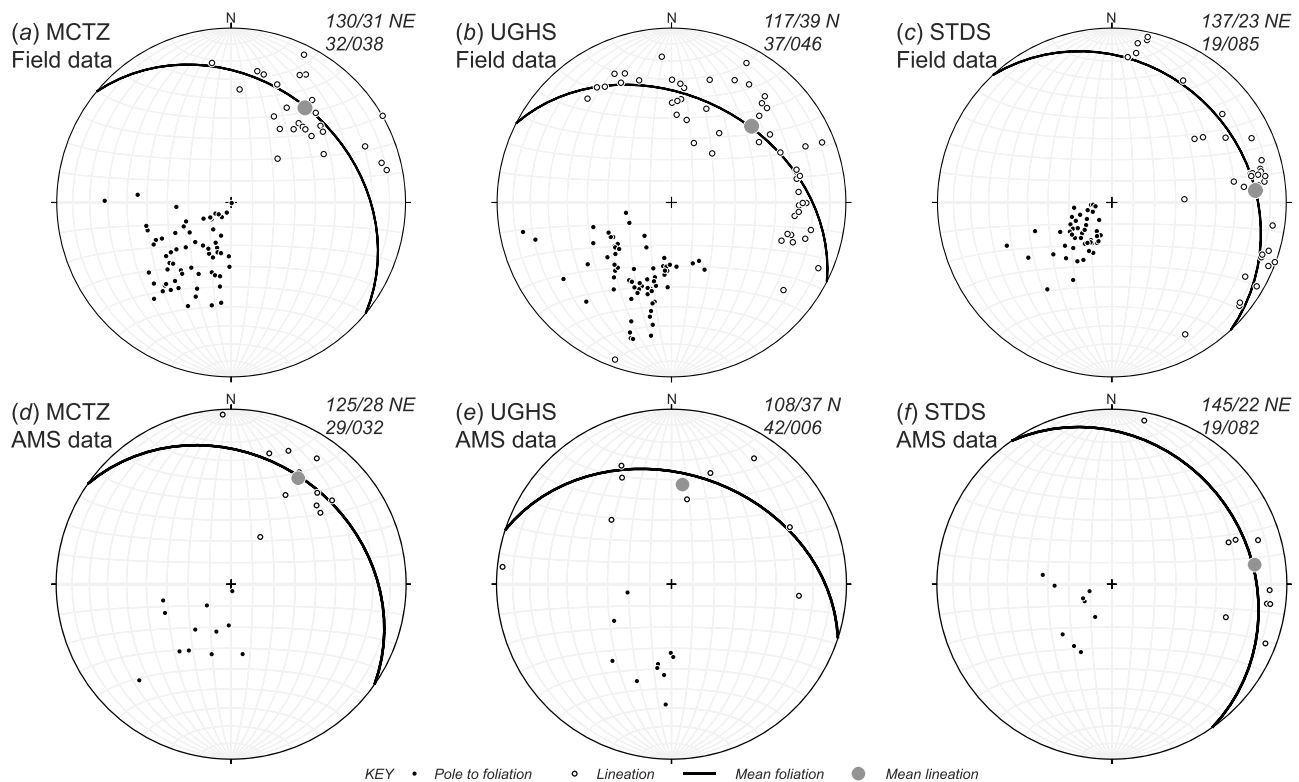


**Figure 5.** Mean AMS and macroscopic grain fabric orientations from the GHS. Macroscopic fabric data for (a) MCTZ, (b) UGHS, and (c) STDS. Mean AMS fabric orientations for (d) MCTZ, (e) UGHS, and (f) STDS. Local macroscopic and AMS fabric orientations are listed in Table 1. Geographically oriented. Plotted using Stereonet 8.0 [Allmendinger et al., 2012].

fabrics across units with variable lithologies, support interpretation of AMS fabrics as a measure of penetrative deformation. AMS principal axis orientations (Table 1 and Figures 4 and S5) of all samples form well-defined magnetic foliations and, in most cases, magnetic lineations (except P12/087M, LHS). A lack of consistent correlation between  $K_m$ ,  $P'$ , and  $T$  (Figure 3) or between magnetic material types,  $P'$  and  $T$  (Figure S6), suggests that AMS varies independently of mineral assemblages. Close correlation is observed between AMS fabric orientation and locally measured deformation fabrics (Table 1 and Figures 2, 4, and 5).

Magnetic lineation ( $K_1$ ) and magnetic foliation ( $K_1$ - $K_2$  great circle) are generally parallel/subparallel to local mineral stretching lineations and macroscopic foliations (Figure 4, Table 1, and Figure S7). In paramagnetic samples, strong correlation is observed between AMS fabric orientations and phyllosilicate CPOs (Figure S3). P13/001M, P13/003M, and P13/048M have *inverse* AMS fabrics [e.g., Potter and Stephenson, 1988; Ferré, 2002], where  $K_3$  forms the magnetic lineation, possibly due to the presence of *uniaxial single domain* (USD) magnetite (see Tauxe [2002] for explanation). P12/052M has an *intermediate* AMS fabric (Intermediate A2 fabric [see Ferré, 2002]) where  $K_2$  forms the magnetic lineation, which may reflect a mixed population of USD-MD magnetite grains (Table 1).

Plotting AMS foliation and lineation orientations on a geological map (Figure 2) and cross sections (Figure S7) strengthens correlation between AMS fabrics and regional structure. AMS fabrics correlate with macroscopic S3 foliation and L3 lineation populations from the GHS [Godin, 2003; Parsons et al., 2016c]. These are shear-related fabrics which overprint and transpose earlier deformation fabrics (Figure S8). Quartz and feldspar CPO fabrics and vorticity analyses of high-temperature S3-L3 fabrics (550°C to >650°C) in the UGHS and base of the STDS record general shear with components of both oblate and plane strain coaxial flattening [Larson and Godin, 2009; Parsons et al., 2016a, 2016b]. AMS fabrics derived from migmatitic samples in the STDS and UGHS may have recorded deformation during partial melting. These correlations between AMS fabrics, S3-L3 macroscopic fabrics, and CPO fabrics [Parsons et al., 2016a, 2016b, 2016c] suggest that AMS fabrics recorded midcrustal deformation kinematics.

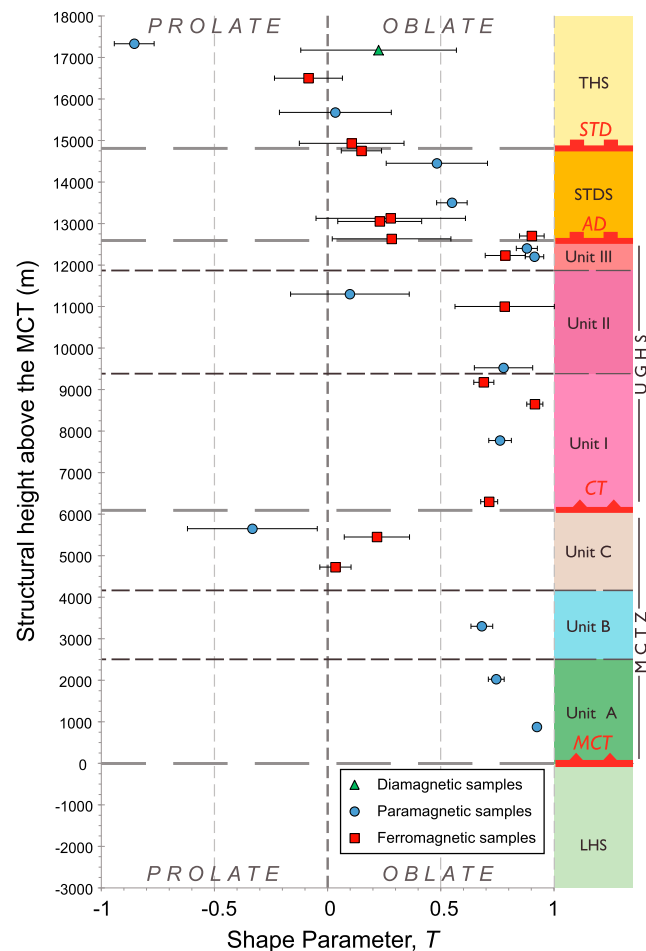


**Figure 6.** Mean AMS ellipsoid shape parameter ( $T$ ) plotted against relative structural height of samples above the MCT. Error bars = 1 standard deviation.

magnetic carriers of different samples vary between phyllosilicate, magnetite, and pyrrhotite, all of which have distinct intrinsic magnetic anisotropies. For example, undeformed magnetite single crystals have an intrinsic  $T$  of  $-0.3$ , while phyllosilicate single crystals have an intrinsic  $T$  ranging from  $0.7$  to  $1.0$  [Tarling and Hrouda, 1993; Martín-Hernández and Hirt, 2003]. The absence of macrostructural and microstructural evidence for two or more crosscutting deformation fabrics indicates that AMS fabrics are not the product of superposition of multiple structural fabrics. Agreement between values of  $T$  from individual specimen cubes of a single sample and the corresponding sample mean  $T$  indicates that planar sample fabrics are not produced by superposition of variably oriented linear fabrics measured in cube specimens. As such, correlation between  $T$  and tectonostratigraphy (Figure 6), independent of magnetic carrier types, suggests that observed variations in  $T$  correspond to variations in strain geometry. This hypothesis is strengthened by correlation between AMS fabric orientations and macroscopic deformation kinematics. We therefore propose that the measured AMS fabrics provide a proxy for 3-D strain geometries and their kinematic interpretation.

## 6. Three-Dimensional Strain Geometries and Kinematic Interpretations

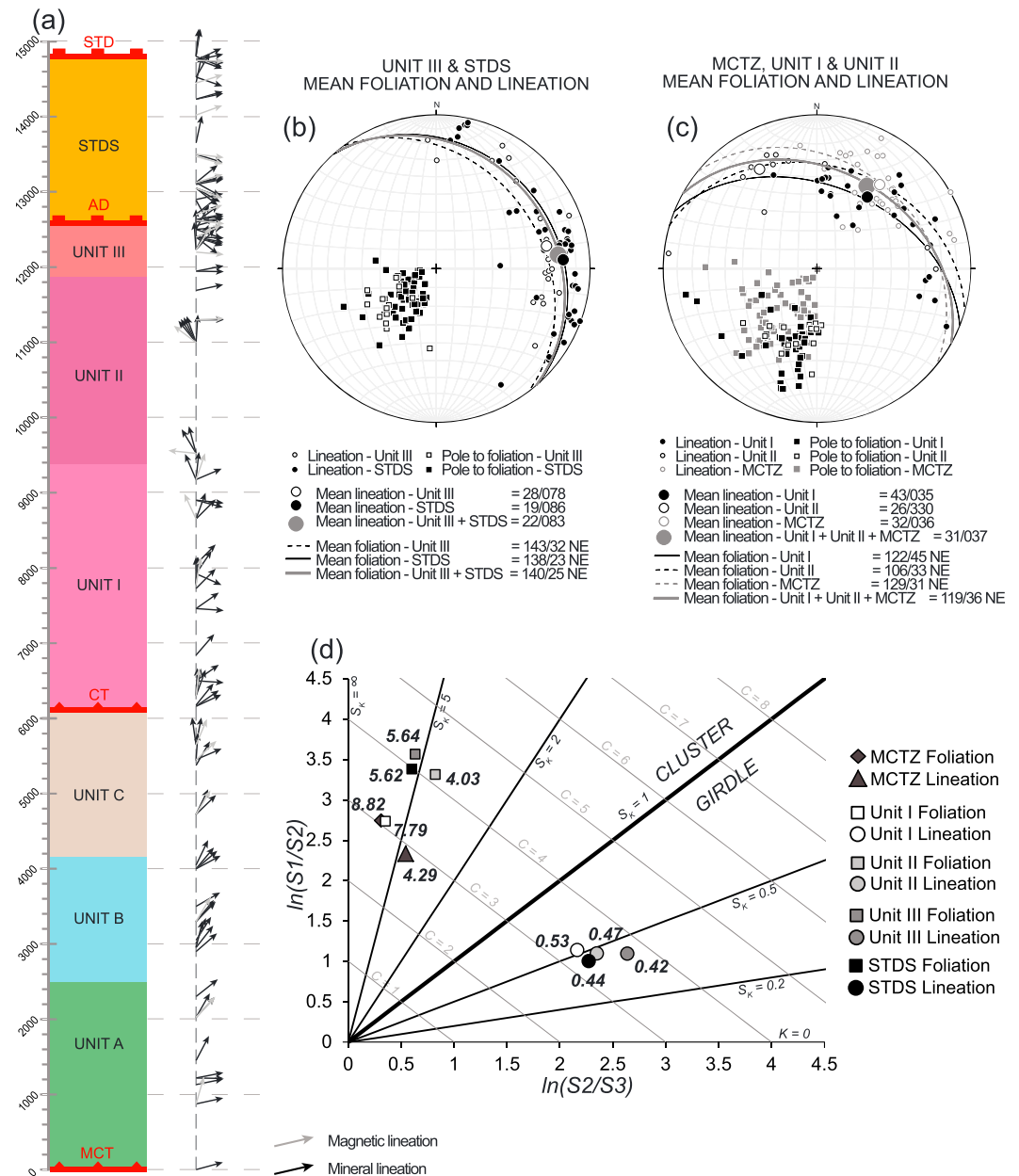
### 6.1. Orogen-Parallel Lineation Azimuths

Figure 7 displays magnetic and macroscopic mineral stretching lineation azimuths and poles to foliation from the MCTZ, UGHS, and STDS. Two distinct trends in lineation azimuth are observed. Mean lineation azimuths in the MCTZ, Unit I, and Unit II range between NNW-NNE on a common great circle striking ESE-WNW (Figure 7c). In Unit III and the STDS, mean lineation azimuths plunge eastward on a common great circle striking SE-NW (Figure 7b). Transition in mean lineation azimuth falls roughly along the boundary between

The AMS fabrics also appear to record variations in 3-D strain geometry. Some authors warn against the use of  $T$  as a proxy for strain geometry as  $T$  also depends on magnetic carrier properties, which is especially the case when measuring AMS of a single specimen cube [e.g., Borradaile and Jackson, 2010; Ferré et al., 2014]. However, sample mean  $T$  was obtained using Anisoft 4.2 [Chadima and Jelinek, 2008] with calculations derived from directional statistics of Jelinek [1978, 1981]. These statistics consider the symmetry of the whole-rock AMS fabric (prolate versus oblate) as a composite of all specimen cube fabrics and are less dependent on mineral properties.

In the MCTZ and LHS, magnetic carrier and  $T$  show a possible correlation (Figures 3b and 6). As such, kinematic interpretations are not made from  $T$  in these units. Samples from the THS, STDS, and UGHS lack correlation between  $T$  and  $K_m$  (Figure 3b) or between magnetic material type and  $T$  (Figure S6b), which suggests that  $T$  varies independently of magnetic mineral assemblage. Importantly, both ferromagnetic and paramagnetic samples in these units produce the same trends in  $T$  over a range of  $T = 0.0$ – $0.9$  (Table 1).

This agreement is significant as the magnetic carriers of different samples vary between phyllosilicate, magnetite, and pyrrhotite, all of which have distinct intrinsic magnetic anisotropies. For example, undeformed magnetite single crystals have an intrinsic  $T$  of  $-0.3$ , while phyllosilicate single crystals have an intrinsic  $T$  ranging from  $0.7$  to  $1.0$  [Tarling and Hrouda, 1993; Martín-Hernández and Hirt, 2003]. The absence of macrostructural and microstructural evidence for two or more crosscutting deformation fabrics indicates that AMS fabrics are not the product of superposition of multiple structural fabrics. Agreement between values of  $T$  from individual specimen cubes of a single sample and the corresponding sample mean  $T$  indicates that planar sample fabrics are not produced by superposition of variably oriented linear fabrics measured in cube specimens. As such, correlation between  $T$  and tectonostratigraphy (Figure 6), independent of magnetic carrier types, suggests that observed variations in  $T$  correspond to variations in strain geometry. This hypothesis is strengthened by correlation between AMS fabric orientations and macroscopic deformation kinematics. We therefore propose that the measured AMS fabrics provide a proxy for 3-D strain geometries and their kinematic interpretation.



**Figure 7.** Linear fabric elements in the GHS. (a) Vertical structural column for the GHS of the Kali Gandaki Valley. Lineation azimuths of macroscopic mineral stretching and AMS lineations plotted at relative structural height above MCT. (b) Macrostructural and AMS orientation data for the STDS and Unit III, UGHS. (c) Macrostructural and AMS fabric orientation data for the MCTZ and Units I and II, UGHS. (d) Linear Flinn plot of eigenvalue analyses. Numbers next to data points correspond to ellipsoid shape,  $S_K$  (equation (4)).  $C$  = fabric strength [Woodcock, 1977]. See text for explanation.

Unit II and Unit III (Figure 7a). Mean lineation azimuths equate to (a) *orogen-perpendicular* stretching in the MCTZ and Units I and II and (b) *orogen-parallel* stretching in Unit III and the STDS.

## 6.2. Oblate AMS Fabrics

Figure 6 summarizes mean  $T$  values for samples from the Kali Gandaki Valley arranged in order of vertical structural position above the MCT. Samples from the Modi Khola Valley (Figure 2) that do not lie along this vertical transect are omitted from the figure, as are samples P13/011M and P13/014M which are faulted out of position. Both ferromagnetic and paramagnetic samples should be present in the same crustal section in order to assess the single crystal intrinsic magnetic properties of phyllosilicate versus magnetite/pyrrhotite



magnetic carriers [Tarling and Hrouda, 1993; Martín-Hernández and Hirt, 2003]. In the UGHS, mean  $T = 0.73$ , suggesting an oblate strain geometry (Figures 3b and 6). In the STDS, mean  $T = 0.41$  (Figure 6), suggesting a suboblate strain geometry (transitional oblate-plane strain; smaller magnitude of stretching parallel to  $Y$  direction, relative to  $X$ ).  $T$  varies little within the UGHS, STDS, and THS but changes sharply across the CT, AD, and STD, suggesting that these units deformed under different 3-D strain geometries.

In some cases, magnetic foliation of oblate AMS sample fabrics is defined by a girdle distribution of cube specimen  $K_1$  and  $K_2$  axes (Figures 4c and 4d, e.g., P13/024M and P13/033M). Within our data set, this type of oblate AMS fabric is found in migmatitic samples containing leucosomes. We suggest that these samples, which yield the most oblate AMS fabrics of the whole sample suite ( $T = 0.9$ ) record synmigmatitic heterogeneous deformation during partial melting and provide the strongest evidence for oblate flattening within the GHS during midcrustal deformation.

### 6.3. Eigenvalue Analysis

The proportionality of cluster to girdle distribution tendencies of a population of linear orientation data can be defined by the eigenvalue statistic,  $K$  [Woodcock, 1977]. To avoid confusion with the magnetic susceptibility (also  $K$ ), we refer to this eigenvalue statistic as  $S_K$ ,

$$S_K = \frac{\ln(S_1/S_2)}{\ln(S_2/S_3)} \quad (4)$$

where  $S_1$ ,  $S_2$ , and  $S_3$  define the maximum, intermediate, and minimum eigenvalues with orthogonal eigenvectors.  $S_K = 0$  defines an axially symmetric girdle distribution.  $S_K \rightarrow \infty$  defines an axially symmetric cluster distribution.  $S_K = 1$  defines a distribution with equal cluster and girdle tendencies [Woodcock, 1977]. Calculating  $S_K$  for populations of macroscopic mineral stretching lineation and pole-to-foliation populations provides constraint on regional strain geometry [e.g., Flinn, 1978; Ramsay and Huber, 1983].

Magnetic and mineral stretching lineations in the MCTZ (Figure 7) have a strong cluster distribution ( $S_K = 4.3$ , Figure 7d) orientated within a common regional foliation plane orientation. This is in agreement with microstructural analyses from the MCTZ that record noncoaxial plane strain [Larson and Godin, 2009; Parsons et al., 2016a]. In contrast, strong girdle distributions of magnetic and mineral stretching lineation populations (Figures 7b and 7c) in the UGHS and STDS ( $S_K = 0.4$ – $0.5$ , Figure 7d) are suggestive of oblate flattening (i.e., nonplane strain). Correlation between microstructural and magnetic fabrics in these units (see section 5) suggest that deformation in the UGHS and STDS reflects a general shear with components of both oblate/suboblate and plane strain coaxial flattening [Larson and Godin, 2009; Parsons et al., 2016a].

## 7. Discussion

### 7.1. Orogen-Parallel Stretching in the GHS

The consistent orientation of pole-to-foliation populations within different tectonostratigraphic units of the GHS (Figures 5, 7b, and 7c) indicates that orogen-parallel lineation azimuths are not the result of late-stage folding or tilting. Correlation with previously published deformation temperature constraints [Parsons et al., 2016a, and references therein] suggests that lineation populations correspond to midcrustal deformation during which pervasive shearing in the STDS and Unit III involved a component of orogen-parallel stretching. In the STDS, deformation had an oblique-top-down-to-ENE normal shear sense associated with a component of right-lateral orogen-parallel stretching within the plane of the low-angle S3 foliation.

Orogen-parallel stretching in the UGHS and STDS is documented regionally, between the Kali Gandaki Valley and the Buhdi Gandaki Valley, ~130 km to the east [Pécher, 1991]. Additionally, both solid-state and magmatic orogen-parallel mineral stretching and AMS lineations are reported from the Manaslu leucogranite pluton and surrounding host rock (UGHS and STDS), ~70 km east of the Kali Gandaki [Guillot et al., 1993; Coleman, 1996]. Elsewhere in the Himalaya (Figure 1), orogen-parallel stretching in the UGHS and STDS is reported in the Zaskar (76°E), Upper Lhaul (77°E), and Garhwal (79°E) regions (western Himalaya) and in the Pulan-Karnali (81°E), Jilong-Nyalam (85–86°E), Ama Drime (87.5°E), Yadong (89°E), and Cuona (90°E) regions (central eastern Himalaya) [Brun et al., 1985; Pécher, 1991; Pécher et al., 1991; Gapais et al., 1992; Guillot et al., 1993; Rochette et al., 1994; Scaillet et al., 1995; Vannay and Steck, 1995; Murphy and Copeland, 2005; Jessup and Cottle, 2010; Xu et al., 2013; Langille et al., 2014; Nagy et al., 2015]. Many of these studies concluded that

deformation of the STDS involved a late-stage component of dextral strike-slip motion during midcrustal extrusion and exhumation of the GHS [Brun *et al.*, 1985; P  cher, 1991; P  cher *et al.*, 1991; Murphy and Copeland, 2005; Xu *et al.*, 2013; Nagy *et al.*, 2015].

## 7.2. Oblate Strain in the GHS

High-temperature macroscopic and microstructural deformation fabrics from the UGHS and STDS are interpreted as a record of midcrustal channel flow [Larson and Godin, 2009; Searle, 2010; Parsons *et al.*, 2016a, 2016b]. As such, our record of inferred strain geometries, some of which correspond to synmigmatitic deformation, suggests that crustal flow in the Annapurna-Dhaulagiri Himalaya occurred under an oblate/suboblate strain regime, involving an orogen-parallel component of stretching. Parsons *et al.* [2016a] also inferred flattening geometries within the UGHS of the Annapurna-Dhaulagiri Himalaya from high-temperature ( $\geq 550$ – $650^\circ\text{C}$ ) quartz and feldspar CPO fabrics.

Three-dimensional crustal flow is proposed in several models for the crustal evolution of the Tibetan Plateau [Dewey *et al.*, 1988; Westaway, 1995; Clark and Royden, 2000; Chen and Gerya, 2016]. Three-dimensional flattening during channel flow in the Himalayan orogen has not been simulated by thermomechanical models as their two-dimensional construct necessitates a plane strain regime [Beaumont *et al.*, 2001, 2004; Jamieson and Beaumont, 2013]. However, the authors of these and similar models have speculated that channel flow could involve a component of oblate strain resulting in simultaneous orogen-perpendicular and orogen-parallel lateral crustal flow [Beaumont *et al.*, 2006, p.135; Culshaw *et al.*, 2006, p. 734].

## 7.3. Orogen-Parallel Midcrustal Deformation During the Himalayan Orogeny

Within the THS of the Kali Gandaki Valley, E-W extension across the Thakkhola graben (Figures 2 and S9) is well documented [Hurtado *et al.*, 2001; Hurtado, 2002; Garzione *et al.*, 2003; Godin, 2003]. The earliest extension recorded along the basin-bounding Dangardzong fault in the upper reaches of the Kali Gandaki Valley occurred prior to 17–18 Ma, as indicated by indistinguishable  $^{40}\text{Ar}/^{39}\text{Ar}$  muscovite ages from amphibolite facies footwall rocks and adjacent weakly metamorphosed hanging wall rocks [Hurtado, 2002]. Importantly, this earliest record of E-W orogen-parallel extension before 17–18 Ma overlaps with the latest record of top-SW orogen-perpendicular synmigmatitic shearing in the UGHS of the Annapurna-Dhaulagiri Himalaya at 18–22 Ma [Nazarchuk, 1993; Hodges *et al.*, 1996; Hurtado, 2002; Iaccarino *et al.*, 2015; Larson and Cottle, 2015]. These time constraints are similar to the earliest record of E-W extensional faulting and fracture development in the THS and STDS of the Manaslu Himalaya at 14–17.5 Ma,  $\sim 70$  km east of the Kali Gandaki [Coleman and Hodges, 1998]. Approximately 170 km northwest of the Kali Gandaki, a transition from orogen-perpendicular to orogen-parallel deformation is recorded in the upper structural levels of the GHS and the overlying THS in the upper Karnali Valley between 13 and 15 Ma [Nagy *et al.*, 2015]. Similarly,  $\sim 230$  km northwest of the Kali Gandaki Valley in the Pulan region of southern Tibet (Figure 1), midcrustal orogen-parallel stretching initiated in the upper structural levels of UGHS-equivalent strata between 15 and 22 Ma [Xu *et al.*, 2013]. In both regions (Figure 1), orogen-parallel deformation initiated at or close to peak metamorphic temperature [Xu *et al.*, 2013; Nagy *et al.*, 2015].

## 7.4. Accommodation of Orogen-Parallel Stretching During Continued Convergence

Radial spreading of the Tibetan plateau during gravitational collapse provides one explanation for E-W extension of southern Tibetan Plateau and Himalayan upper crust [Styron *et al.*, 2011]. An additional or alternative explanation is provided by models of strain partitioning in response to obliquity between northward motion of the Indian Plate and the arcuate orogenic strike of the Himalaya [McCaffrey and Nabelek, 1998; Styron *et al.*, 2011]. Earthquake focal mechanisms along the length of the Himalayan frontal thrust system record thrust motions perpendicular to local orogenic strike, while GPS vectors indicate that the motion of the Indian Plate is only normal to the orogenic strike in the Everest region (Figure 1) [Styron *et al.*, 2011]. Obliquity between the Indian Plate motion and slip vectors on orogen-perpendicular thrust faults increases along strike from the Everest region toward the east and west syntaxes [Styron *et al.*, 2011]. In order to maintain strain compatibility during oblique convergence, displacement vectors are partitioned into orogen-perpendicular convergence on the frontal thrust system and orogen-parallel stretching and extension on hinterland strike-slip and normal faults [McCaffrey and Nabelek, 1998; Styron *et al.*, 2011; Murphy *et al.*, 2014; Whipp *et al.*, 2014; Silver *et al.*, 2015; Wallis *et al.*, 2015].

In the Annapurna-Dhaulagiri region, obliquity between the Indian Plate motion and orogenic strike is  $\sim 15^\circ$  [cf. *Styron et al.*, 2011]. Seventy kilometers west of the Annapurna-Dhaulagiri region, strain partitioning is suggested to be responsible for development of the Western Nepal Fault System (WNFS), which links the hinterland Karakoram Fault Zone to the frontal thrust system south of Annapurna (Figure 1) [*Murphy et al.*, 2014; *Wallis et al.*, 2014b; *Silver et al.*, 2015]. As yet, a kinematic link between the WNFS and the Thakkhola graben has not been identified at ground level; however, given the proximity of these structures, it is possible that the two systems formed in response to the same stress regime.

Current channel flow models are implicitly two-dimensional [e.g., *Beaumont et al.*, 2001, 2004; *Grujic*, 2006]. In these models, the direction of the lateral pressure gradient produced by the overburden of the Tibetan Plateau is diametrically opposed to the motion of the underthrusting Indian Plate (i.e., pressure gradient and plate motion are parallel but with opposite directions). This, by default, simulates channel flow in plane strain. In reality, the Indian Plate motion remains constant along the length of the orogen, while the direction of the opposing overburden-induced lateral pressure gradient rotates to maintain an orogen-perpendicular orientation, reflecting the radial gravitational spreading of the Tibetan Plateau [e.g., *Brun and Merle*, 1985; *Merle*, 1989]. In regions where the Indian Plate motion and the overburden-induced pressure gradient are obliquely opposed (i.e., nonparallel), the combined shear of these two forces will not produce a plane strain but will instead produce an oblate/suboblate strain. We suggest that in these regions, *prior* to upper crustal orogen-parallel extension, pervasive oblate flattening of the active channel flow accommodated oblique convergence within the channel, without the need for orogen-scale partitioning of deformation into orogen-perpendicular and orogen-parallel displacement vectors.

Evidence for midcrustal orogen-parallel stretching of the GHS continues to grow; however, it remains unclear as to how this deformation was/is accommodated at the orogen scale. Some authors suggest that orogen-parallel stretching within the GHS is accommodated by orogen-parallel transportation of material into the east and west syntaxes where deformation is characterized by horizontal shortening and vertical stretching [*McCaffrey and Nabelek*, 1998; *Butler et al.*, 2002; *Whipp et al.*, 2014]. Alternatively, orogen-parallel stretching may have been and may still be restricted on a regional scale to oblate strain domains separated by transport-parallel prolate/plane strain domains [e.g., *Sylvester and Janecky*, 1988; *Law*, 2010], in response to radial spreading of the GHS and Tibetan midcrust [e.g., *Brun and Merle*, 1985; *Merle*, 1989]. Alternation between oblate and prolate/plane strain domains may occur along orogenic strike. Alternatively, oblate strain domains may be confined to the top of the GHS (i.e., the UGHS), while prolate/plane strain domains may be confined to the base of the GHS (i.e., the MCTZ) [e.g., *Merle*, 1989, Figure 8]. Similar models of orogen-parallel stretching and oblate flattening driven by gravitational radial spreading or oroclinal bending have been proposed for the Hudson Highlands [*Gates*, 1996], European Alps [*Ratschbacher et al.*, 1991; *Ring*, 1992], Carpathians [*Schmid et al.*, 1998; *Jeřábek et al.*, 2007], Betics [*Williams and Platt*, 2013], Sveconorwegian Orogen [*Viola and Henderson*, 2010], and Caledonides [*Hossack and Cooper*, 1986; *Ellis and Watkinson*, 1987; *Sylvester and Janecky*, 1988].

In the Himalaya, along-strike alternating oblate and prolate/plane strain domains provide plausible explanation for the regional-scale along-strike distribution of  $\text{km}^3$  scale accumulations of leucogranite at intervals of  $\sim 50$ – $100$  km (Figure 1), separated by regions that are comparatively depleted in leucogranite [*Parsons et al.*, 2016b, and references therein]. In this situation, regional domains of oblate flattening strains may have driven orogen-parallel melt migration toward prolate/plane strain domains. Orogen-parallel magmatic lineations in the Manaslu leucogranite support the concept of orogen-parallel melt migration [*Guillot et al.*, 1993; *Coleman*, 1996]. In the Garhwal Himalaya, *Scaillet et al.* [1995] made similar interpretations from field-macrostructural and AMS analyses of the Gangotri granite (Figure 1). These authors suggest that  $\text{km}^3$  scale tabular laccoliths of the Gangotri granite represent crustal-scale boudins, which formed during oblate coaxial deformation [*Rochette et al.*, 1994; *Scaillet et al.*, 1995]. Additionally, kinematically distinct regional-scale deformation domains are proposed for the present-day crustal structure of the Tibetan Plateau, based on the spatial variation of seismic anisotropy [*Sherrington et al.*, 2004].

### 7.5. Transition of Deformation Modes

Numerous studies from across the Himalaya have recorded a transition from orogen-perpendicular extrusion of the GHS to orogen-parallel stretching and extensional and strike-slip faulting between the THS and GHS at  $\sim 13$ – $22$  Ma [*Coleman and Hodges*, 1995; *Coleman*, 1996; *Coleman and Hodges*, 1998;

Hurtado, 2002; Jessup *et al.*, 2008; Jessup and Cottle, 2010; Styron *et al.*, 2011; Xu *et al.*, 2013; Langille *et al.*, 2014; Nagy *et al.*, 2015]. It is likely that mineral stretching lineations in the UGHS and the STDS correspond only to the final stage of midcrustal deformation during which high-temperature deformation microstructures are set in [e.g., Knipe and Law, 1987; Parsons *et al.*, 2016a]. As such, orogen-parallel stretching lineations in Unit III and the STDS may record the initial transition from midcrustal orogen-perpendicular extrusion of the UGHS to middle to upper crustal orogen-parallel extension and dextral transtension of the THS and upper portion of the GHS, during the mid-Miocene [Styron *et al.*, 2011; Xu *et al.*, 2013; Nagy *et al.*, 2015].

We note that in the Annapurna-Dhaulagiri-Manaslu Himalaya and neighboring regions, the earliest records of E-W extension [e.g., Coleman and Hodges, 1998; Hurtado *et al.*, 2001; Hurtado, 2002; Xu *et al.*, 2013; Nagy *et al.*, 2015] overlap with the cessation of midcrustal flow/pervasive shearing of the GHS which came to an end between 25 and 18 Ma [Parsons *et al.*, 2016b, and references therein] but possibly began to shut down as early as ~30 Ma [Carosi *et al.*, 2016]. We also note that the timing of this transition overlaps with emplacement of the Mustang and Mugu granite plutons in the northern reaches of the Kali Gandaki Valley, (Figure S9) at ~24–23 Ma and ~21–17 Ma, respectively, and emplacement of the Manaslu leucogranite pluton at 22–19 Ma [Harrison *et al.*, 1997; Guillot *et al.*, 1999; Harrison *et al.*, 1999; Hurtado, 2002; Hurtado *et al.*, 2007]. The Mustang and Mugu granites (Figure S9) form the mylonitized footwall to the Dangardzong fault along the western margin of the Thakkhola graben [Harrison *et al.*, 1997; Guillot *et al.*, 1999; Hurtado *et al.*, 2001; Hurtado, 2002]. The Manaslu leucogranite pluton and surrounding country rock preserve orogen-parallel magmatic and solid-state mineral stretching lineations, as identified from field macrostructures and rock magnetic fabrics [Guillot *et al.*, 1993; Coleman, 1996]. Consequently, we suggest that in this region, the cessation of midcrustal flow, leucogranite pluton emplacement, and initiation of orogen-parallel stretching at mid-crustal levels were kinematically linked. We propose that existing timing constraints indicate a cause and effect relationship between the *cessation* of crustal flow and the *initiation* of orogen-parallel extension, such that the two processes could not be effectively maintained simultaneously.

During cessation of flow, the channel strengthened to form a *channel plug* which mechanically *recoupled* the upper, middle, and lower crustal units by removing any rheological contrast between the channel and channel walls [Parsons *et al.*, 2016b]. Orogen-parallel melt extraction from the Annapurna-Dhaulagiri Himalaya may have promoted the cessation of channel flow in this region and also provides an explanation for the lower-than-typical thickness of the UGHS (7 km), relative to other regions (10–30 km) in the Himalaya [Parsons *et al.*, 2016b]. Following mechanical strengthening and recoupling, oblique convergence could no longer be accommodated through pervasive oblate strain of the UGHS. Subsequently, continued oblique convergence required strain partitioning in the upper crust between thrust faults and normal and strike-slip faults to maintain strain compatibility [e.g., Styron *et al.*, 2011].

We note that the position of the kinematic discontinuity between Unit II and Unit III lineation orientations is coincident with the top-SW Kalopani Shear Zone [Vannay and Hodges, 1996; Carosi *et al.*, 2016]. We also recognize a potential discontinuity between north to east plunging lineations in Unit I and north to northwest plunging lineations in Unit II (Figure 7). Similar kinematic discontinuities between orogen-perpendicular and orogen-parallel stretching directions within the GHS have been mapped elsewhere along the Himalaya [Pécher *et al.*, 1991; Xu *et al.*, 2013]. In many cases, these discontinuities are also *metamorphic* in nature and can be observed in the field as reverse sense shear zones, some of which lie coincident with the sillimanite-in isograd [Pécher *et al.*, 1991; Xu *et al.*, 2013; Montomoli *et al.*, 2015; Mukherjee, 2015]. It is possible that these discontinuities aided the partitioning of orogen-perpendicular and orogen-parallel stretching following the cessation of crustal flow and pervasive shearing of the GHS [cf. Montomoli *et al.*, 2015; Carosi *et al.*, 2016].

We suggest that similar deformation sequences occurred elsewhere in the Himalaya, where the GHS can be divided into portions of orogen-perpendicular and orogen-parallel stretching [e.g., Brun *et al.*, 1985; Pécher, 1991; Pécher *et al.*, 1991; Xu *et al.*, 2013]. These models require further investigation to assess their validity, but they do provide coherent reasoning for why the two deformation modes (midcrustal flow/extrusion and upper crustal extension) were not sustained simultaneously. Additionally, while a cause and effect relationship appears to exist between the cessation of flow and the initiation of orogen-parallel extension, it is not clear which is the cause and which is the effect. It is possible that an external factor provided the catalysts to start the transition in deformation modes. This transition is reported from multiple locations along the

Himalaya between 22 and 13 Ma [see *Nagy et al.*, 2015, and references therein] and may reflect a major change in the boundary conditions governing the Himalaya-Tibet orogenic system. We support the proposal of *Nagy et al.* [2015] who suggest that this transition in deformation modes reflects a change in the balance of forces across the orogenic system between ~20 and 10 Ma, caused by one or more of the following events: (1) an increase in the mean elevation of the Tibetan Plateau, (2) the removal of mantle lithosphere beneath the Tibetan Plateau, (3) the onset of eastward crustal flow of the Tibetan lower crust, and (4) a 35–45% decrease in convergence rate between Indian and Eurasia [Westaway, 1995; Clark and Royden, 2000; Royden et al., 2008; Molnar and Stock, 2009; Searle et al., 2011; Iaffaldano et al., 2013]. Such events highlight the importance of considering the rheological and mechanical boundary conditions of Composite Orogenic Systems in three dimensions [Parsons et al., 2016a].

## 8. Conclusions

Integrated AMS and structural analyses have been conducted across the Greater Himalayan Sequence (GHS) and bounding units in the Kali Gandaki Valley of the Annapurna-Dhaulagiri Himalaya, central Nepal. AMS analysis of 40 samples, accompanied by magnetic hysteresis and FORC analyses, reveals that magnetite, pyrrhotite, and phyllosilicate form the magnetic carriers of most samples. Consideration of magnetic carrier properties demonstrates a clear correlation between AMS and deformation fabrics and supports the use of these AMS fabrics as proxies for 3-D strain geometries and their kinematic interpretation. Correlation with previously published constraints indicates that AMS fabrics from the UGHS and base of the STDS provide a record of high-temperature, synmigmatitic to postmigmatitic deformation (>550–650°C).

Magnetic and mineral stretching lineations record orogen-perpendicular stretching in the MCTZ and Units I and II of the UGHS and are structurally overlain by orogen-parallel stretching in the STDS and Unit III of the UGHS. Shape parameter ( $T$ ) analyses of AMS ellipsoids and eigenvalue analyses of lineation populations suggest that these data represent plane strain proxies in the MCTZ and oblate/suboblate strain proxies in the UGHS and STDS. The most oblate AMS ellipsoids ( $T=0.9$ ), which are recorded in migmatitic samples, correspond to synmigmatitic heterogeneous deformation under an oblate strain regime.

We interpret these data as an indication that channel flow in the Annapurna-Dhaulagiri Himalaya occurred under an oblate/suboblate strain regime. We propose that prior to upper crustal orogen-parallel extension, midcrustal oblate/suboblate strain during channel flow accommodated the obliquity between northward Indian Plate motion and the lateral pressure gradient induced by the overburden of the Tibetan Plateau and orientated perpendicular to the arcuate orogenic front.

Midcrustal orogen-parallel stretching and oblate flattening may have been accommodated through transportation of crustal material into the east and west syntaxes [e.g., Whipp et al., 2014] or by development of regional-scale oblate strain domains between prolate/plane strain domains [e.g., Sylvester and Janecky, 1988; Merle, 1989; Law, 2010]. The latter hypothesis may have promoted development of melt-depleted regions between km<sup>3</sup> scale leucogranite plutons emplaced at 50–100 km intervals along the length of orogen, via orogen-parallel melt migration.

During cessation of crustal flow, rheological strengthening of the UGHS and mechanical *recoupling* of the upper and lower crusts resulted in the initiation of upper crustal orogen-parallel extension as a means to maintain strain compatibility during continued oblique convergence. Timing constraints from the Annapurna-Dhaulagiri Himalaya and neighboring regions suggest that midcrustal flow and upper crustal orogen-parallel extension could not be effectively sustained simultaneously. We suggest that cessation of midcrustal flow/pervasive shearing and initiation of orogen-parallel extension share a “cause and effect” relationship such that the occurrence of one promoted the occurrence of the other. It is unclear which process occurred first, and it is possible that an external factor provided the catalyst to start the transition in deformation modes. We favor the proposal of *Nagy et al.* [2015] who suggest that an orogen-wide transition in deformation modes occurred in response to a change in balance of forces across the orogenic system between ~10 and 20 Ma. High-temperature orogen-parallel magnetic and mineral stretching lineations in the STDS and upper UGHS record the initial transition between deformation modes in the Annapurna-Dhaulagiri Himalaya.

Lastly, our 3-D strain observations cannot be accounted for by current numerical simulations of Himalayan midcrustal deformation due to their 2-D nature that implicitly simulates plane strain deformation.



Importantly, midcrustal orogen-parallel deformation within Composite Orogenic Systems [Parsons et al., 2016a] will have significant implications for rates of convergence, extrusion, exhumation, fluid flow, melt migration, heat advection, and the forces that balance them. Further efforts should be made to incorporate orogen-parallel deformation into tectonic models of Himalayan orogenesis.

## Acknowledgments

Reviews and comments from an anonymous reviewer, Teresa Román-Berdiel, and Associate Editor Augusto Rapalini helped improve this manuscript. Suka Ghale, Basan Sherpa, and their Nepalese colleagues are thanked for their assistance during fieldwork. Dave Wallis (University of Oxford) provided helpful discussion during write-up. Research was supported by the Natural Environment Research Council (training grant NE/J50001X/1) and the Geological Society of London (Elspeth Matthews Research Fund) to A.J.P. and National Science Foundation grant EAR0711207 to R.D.L. Rock magnetism analyses were conducted on instrumentation acquired through National Science Foundation grant EAR0521558 to E.C.F. Research Councils UK funded open access publication. Data used are listed in the references, tables, and supporting information.

## References

- Allmendinger, R. W., N. Cardozo, and D. M. Fisher (2012), *Structural Geology Algorithms: Vectors and Tensors*, Cambridge Univ. Press, New York.
- Antolin, B., E. Appel, C. Montomoli, I. Dunkl, L. Ding, R. Gloaguen, and R. El Bay (2011), Kinematic evolution of the eastern Tethyan Himalaya: Constraints from magnetic fabric and structural properties of the Triassic flysch in SE Tibet, in *Kinematic Evolution and Structural Styles of Fold-and-Thrust Belts*, edited by J. Poblet and R. J. Lisle, *Geol. Soc. Spec. Publ.*, 349, 99–121.
- Avouac, J. P. (2015), Mountain building: From earthquakes to geologic deformation, in *Treatise on Geophysics*, vol. 6, edited by G. Schubert, pp. 238–432, Elsevier, Oxford.
- Bachmann, F., R. Hielscher, and H. Schaeben (2010), Texture analysis with MTEX—free and open source software toolbox, *Solid State Phenom.*, 160, 63–68, doi:10.4028/www.scientific.net/SSP.160.63.
- Beaumont, C., R. A. Jamieson, M. H. Nguyen, and B. Lee (2001), Himalayan tectonics explained by extrusion of a low-viscosity crustal channel coupled to focused surface denudation, *Nature*, 414(6865), 738–742.
- Beaumont, C., R. A. Jamieson, M. H. Nguyen, and S. Medvedev (2004), Crustal channel flows: 1. Numerical models with applications to the tectonics of the Himalayan-Tibetan orogen, *J. Geophys. Res.*, 109, B06406, doi:10.1029/2003JB002809.
- Beaumont, C., M. H. Nguyen, R. A. Jamieson, and S. Ellis (2006), Crustal flow modes in large hot orogens, in *Channel Flow, Ductile Extrusion and Exhumation in Continental Collision Zones*, edited by R. D. Law, M. P. Searle, and L. Godin, *Geol. Soc. Spec. Publ.*, 268, 91–145.
- Benn, K. (1994), Overprinting of magnetic fabrics in granites by small strains: Numerical modelling, *Tectonophysics*, 233, 153–162.
- Borradaile, G. J. (1991), Correlation of strain with anisotropy of magnetic-susceptibility (AMS), *Pure Appl. Geophys.*, 135, 15–29.
- Borradaile, G. J., and M. Jackson (2004), Anisotropy of magnetic susceptibility (AMS): Magnetic petrofabrics of deformed rocks, in *Magnetic Fabric: Methods and Applications*, edited by F. Martín-Hernández et al., *Geol. Soc. Spec. Publ.*, 238, 299–360.
- Borradaile, G. J., and M. Jackson (2010), Structural geology, petrofabrics and magnetic fabrics (AMS, AARM, AIRM), *J. Struct. Geol.*, 32, 1519–1551, doi:10.1016/j.jsg.2009.09.006.
- Bouchez, J.-L., and A. Pêcher (1981), The Himalayan Main Central Thrust pile and its quartz-rich tectonites in central Nepal, *Tectonophysics*, 78, 23–50.
- Britton, T. B., J. Jiang, Y. Guo, A. Vilalta-Clemente, D. Wallis, L. N. Hansen, A. Winkelmann, and A. J. Wilkinson (2016), Tutorial: Crystal orientations and EBSD—Or which way is up?, *Mater. Charact.*, 117, 113–126, doi:10.1016/j.matchar.2016.04.008.
- Brun, J.-P., and O. Merle (1985), Strain patterns in models of spreading-gliding nappes, *Tectonics*, 4, 705–719, doi:10.1029/TC004i007p00705.
- Brun, J.-P., J.-P. Burg, and C. G. Ming (1985), Strain trajectories above the Main Central Thrust (Himalaya) in southern Tibet, *Nature*, 313, 388–390, doi:10.1038/313388a0.
- Burchfiel, B. C., Z. Chen, K. V. Hodges, Y. Liu, L. H. Royden, C. Deng, and J. Xu (1992), The South Tibetan Detachment System, Himalayan Orogen: Extension contemporaneous with and parallel to shortening in a collisional mountain belt, *Geol. Soc. Am., Spec. Pap.*, 269, 1–41.
- Butler, R. W. H., M. Casey, G. E. Lloyd, C. E. Bond, P. Mcdade, Z. Shipton, and R. Jones (2002), Vertical stretching and crustal thickening at Nanga Parbat, Pakistan Himalaya: A model for distributed continental deformation during mountain building, *Tectonics*, 21, 1–17, doi:10.1029/2001TC901022.
- Carosi, R., L. Gemignani, L. Godin, S. Iaccarino, K. Larson, C. Montomoli, and S. Rai (2014), A geological journey through the deepest gorge on Earth: the Kali Gandaki valley section, central Nepal, in *Geological field trips in the Himalaya, Karakoram and Tibet*, edited by C. Montomoli et al., *J. Virtual Explorer.*, 47.
- Carosi, R., C. Montomoli, A. Langone, A. Turina, B. Cesare, S. Iaccarino, L. Fascioli, D. Visonà, A. Ronchi, and S. M. Rai (2015), Eocene partial melting recorded in peritectic garnets from kyanite-gneiss, Greater Himalayan Sequence, central Nepal, in *Tectonics of the Himalaya*, edited by S. Mukherjee et al., *Geol. Soc. Spec. Publ.*, 412, 111–129.
- Carosi, R., C. Montomoli, S. Iaccarino, H.-J. Massonne, D. Rubatto, A. Langone, L. Gemignani, and D. Visonà (2016), Middle to late Eocene exhumation of the Greater Himalayan Sequence in the Central Himalayas: Progressive accretion from the Indian plate, *Geol. Soc. Am. Bull.*, doi:10.1130/B31471.1.
- Chadima, M., and V. Jelinek (2008), Anisofit 4.2.—Anisotropy data browser, in *Paleo, Rock and Environmental Magnetism, 11th Castle Meeting, Contribution to Geophysics and Geodesy, Special issue*, vol. 41, *Geophys. Inst. of the Slovak Acad. of Sci., Bojnice Castle, Slovak Republic*.
- Chen, L., and T. V. Gerya (2016), The role of lateral lithospheric strength heterogeneities in orogenic plateau growth: Insights from 3-D thermo-mechanical modeling, *J. Geophys. Res. Solid Earth*, 121, 3118–3138, doi:10.1002/2016JB012872.
- Clark, M. K., and L. H. Royden (2000), Topographic ooze: Building the eastern margin of Tibet by lower crustal flow, *Geology*, 28, 703–706.
- Coleman, M., and K. Hodges (1995), Evidence for Tibetan Plateau uplift before 14 Myr ago from a new minimum age for east-west extension, *Nature*, 374, 49–52.
- Coleman, M. E. (1996), Orogen-parallel and orogen-perpendicular extension in the central Nepalese Himalayas, *Geol. Soc. Am. Bull.*, 108, 1594–1607.
- Coleman, M. E., and K. V. Hodges (1998), Contrasting Oligocene and Miocene thermal histories from the hanging wall and footwall of the South Tibetan Detachment in the central Himalaya from  $^{40}\text{Ar}/^{39}\text{Ar}$  thermochronology, Marsyandi Valley, central Nepal, *Tectonics*, 17, 726–740, doi:10.1029/98TC02777.
- Cottle, J. M., K. P. Larson, and D. A. Kellett (2015), How does the mid-crust accommodate deformation in large, hot collisional orogens? A review of recent research in the Himalayan orogen, *J. Struct. Geol.*, 78, 119–133, doi:10.1016/j.jsg.2015.06.008.
- Culshaw, N. G., C. Beaumont, and R. A. Jamieson (2006), The orogenic superstructure-infrastructure concept: Revisited, quantified, and revived, *Geology*, 34, 733–736, doi:10.1130/g22793.1.
- Dewey, J. F., R. M. Shackleton, C. Chang, and Y. Sun (1988), The tectonic evolution of the Tibetan Plateau, *Philos. Trans. R. Soc., A*, 327, 379–413, doi:10.1098/rsta.1988.0135.
- Dunlop, D. J. (2002a), Theory and application of the Day plot ( $M_s/M_d$  versus  $H_c/H_d$ ): 1. Theoretical curves and tests using titanomagnetite data, *J. Geophys. Res.*, 107, 1–22, doi:10.1029/2001JB000486.

- Dunlop, D. J. (2002b), Theory and application of the Day plot ( $M_r/M_s$  versus  $H_c/H_c$ ): 2. Application to data for rocks, sediments, and soils, *J. Geophys. Res.*, **107**(B3), 2057, doi:10.1029/2001JB000487.
- Ellis, M., and A. J. Watkinson (1987), Orogen-parallel extension and oblique tectonics: The relation between stretching lineations and relative plate motions, *Geology*, **15**, 1022–1026, doi:10.1130/0091-7613(1987)15<1022:OEAOOT>2.0.CO;2.
- Ferré, E. C. (2002), Theoretical models of intermediate and inverse AMS fabrics, *Geophys. Res. Lett.*, **29**(7), 1127, doi:10.1029/2001GL014367.
- Ferré, E. C., G. Gleizes, M. T. Djouadi, J. L. Bouchez, and F. X. O. Ugodulunwa (1997), Drainage and emplacement of magmas along an inclined transcurrent shear zone: Petrophysical evidence from a granite-charnockite pluton (Rahama, Nigeria), in *Granite: From Segregation of Melt to Emplacement Fabrics*, *Petrol. Struct. Geol.*, vol. 8, edited by J. L. Bouchez, D. H. W. Hutton, and W. E. Stephens, pp. 253–273, Kluwer, Dordrecht.
- Ferré, E. C., C. Teyssier, M. Jackson, J. W. Thill, and E. S. G. Rainey (2003), Magnetic susceptibility anisotropy: A new petrofabric tool in migmatites, *J. Geophys. Res.*, **108**(B2), 2086, doi:10.1029/2002JB001790.
- Ferré, E. C., F. Martín-Hernández, C. Teyssier, and M. Jackson (2004), Paramagnetic and ferromagnetic anisotropy of magnetic susceptibility in migmatites: Measurements in high and low fields and kinematic implications, *Geophys. J. Int.*, **157**, 1119–1129, doi:10.1111/j.1365-246X.2004.02294.x.
- Ferré, E. C., A. Gëbelin, J. L. Till, C. Sassi, and K. C. Burmeister (2014), Deformation and magnetic fabrics in ductile shear zones: A review, *Tectonophysics*, **629**, 179–188, doi:10.1016/j.tecto.2014.04.008.
- Ferré, E. C., Y.-M. Chou, R. L. Kuo, E.-C. Yeh, N. R. Leibovitz, A. L. Meado, L. Campbell, and J. W. Geissman (2016), Deciphering viscous flow of frictional melts with the mini-AMS method, *J. Struct. Geol.*, **90**, 15–26, doi:10.1016/j.jsg.2016.07.002.
- Flinn, D. (1978), Construction and computation of three-dimensional progressive deformations, *J. Geol. Soc.*, **135**, 291–305.
- Gapais, D., A. Pêcher, E. Gilbert, and M. Ballèvre (1992), Synconvergence spreading of the higher Himalaya crystalline in Ladakh, *Tectonics*, **11**, 1045–1056, doi:10.1029/92TC00819.
- Garzone, C. N., P. G. Decelles, D. G. Hodkinson, T. P. Ojha, and B. N. Upreti (2003), East-west extension and Miocene environmental change in the southern Tibetan Plateau: Thakkhola graben, central Nepal, *Geol. Soc. Am. Bull.*, **115**, 3–20, doi:10.1130/0016-7606(2003)115<0003:eweame>2.0.co;2.
- Gates, A. E. (1996), Megaboudins and lateral extension along the leading edge of a crystalline thrust sheet, Hudson Highlands, New York, U.S. A, *J. Struct. Geol.*, **18**, 1205–1216, doi:10.1016/S0191-8141(96)00043-0.
- Godin, L. (2003), Structural evolution of the Tethyan sedimentary sequence in the Annapurna area, central Nepal Himalaya, *J. Asian Earth Sci.*, **22**, 307–328, doi:10.1016/S1367-9120(03)00066-X.
- Godin, L., R. R. Parrish, R. L. Brown, and K. V. Hodges (2001), Crustal thickening leading to exhumation of the Himalayan metamorphic core of central Nepal: Insight from U-Pb geochronology and  $^{40}\text{Ar}/^{39}\text{Ar}$  thermochronology, *Tectonics*, **20**, 729–747, doi:10.1029/2000TC001204.
- Goscombe, B., D. Gray, and M. Hand (2006), Crustal architecture of the Himalayan metamorphic front in eastern Nepal, *Gondwana Res.*, **10**, 232–255, doi:10.1016/j.gr.2006.05.003.
- Grasemann, B., H. Fritz, and J. C. Vannay (1999), Quantitative kinematic flow analysis from the Main Central Thrust Zone (NW-Himalaya, India): Implications for a decelerating strain path and the extrusion of orogenic wedges, *J. Struct. Geol.*, **21**, 837–853.
- Green, O. R., M. P. Searle, R. I. Corfield, and R. M. Corfield (2008), Cretaceous-Tertiary carbonate platform evolution and the age of the India-Asia collision along the Ladakh Himalaya (Northwest India), *J. Geol.*, **116**, 331–353, doi:10.1086/588831.
- Grujic, D. (2006), Channel flow and continental collision tectonics: An overview, in *Channel Flow, Ductile Extrusion and Exhumation in Continental Collision Zones*, *Geol. Soc. Spec. Publ.*, vol. 268, edited by R. D. Law, M. P. Searle, and L. Godin, pp. 25–37.
- Guillot, S., A. Pêcher, P. Rochette, and P. Le Fort (1993), The emplacement of the Manaslu granite of central Nepal: Field and magnetic susceptibility constraints, in *Himalayan Tectonics*, edited by P. J. Treloar and M. P. Searle, *Geol. Soc. Spec. Publ.*, **74**, 413–428.
- Guillot, S., M. Cosca, P. Allemand, and P. Le Fort (1999), Contrasting metamorphic and geochronologic evolution along the Himalayan belt, in *Himalaya and Tibet: Mountain Roots to Mountain Tops*, edited by A. Macfarlane, R. B. Sorkhabi, and J. Quade, *Geol. Soc. Am. Spec. Pap.*, **328**, 117–128.
- Hargraves, R. B., D. Johnson, and C. Y. Chan (1991), Distribution anisotropy: The cause of AMS in igneous rocks?, *Geophys. Res. Lett.*, **18**, 2193–2196, doi:10.1029/91GL01777.
- Harrison, R. J., and J. M. Feinberg (2008), FORCinel: An improved algorithm for calculating first-order reversal curve distributions using locally weighted regression smoothing, *Geochem. Geophys. Geosyst.*, **9**, Q05016, doi:10.1029/2008GC001987.
- Harrison, T. M., O. M. Lovera, and M. Grove (1997), New insights into the origin of two contrasting Himalayan granite belts, *Geology*, **25**, 899–902.
- Harrison, T. M., M. Grove, K. D. McKeegan, C. D. Coath, O. M. Lovera, and P. Le Fort (1999), Origin and episodic emplacement of the Manaslu intrusive complex, central Himalaya, *J. Petrol.*, **40**, 3–19.
- He, D., A. A. G. Webb, K. P. Larson, A. J. Martin, and A. K. Schmitt (2014), Extrusion vs. duplexing models of Himalayan mountain building: 3. Duplexing dominates from the Oligocene to present, *Int. Geol. Rev.*, **57**, 1–27, doi:10.1080/00206814.2014.986669.
- Herman, F., et al. (2010), Exhumation, crustal deformation, and thermal structure of the Nepal Himalaya derived from the inversion of thermochronological and thermobarometric data and modeling of the topography, *J. Geophys. Res.*, **115**, B06407, doi:10.1029/2008JB006126.
- Hodges, K. V., R. R. Parrish, and M. P. Searle (1996), Tectonic evolution of the central Annapurna Range, Nepalese Himalayas, *Tectonics*, **15**, 1264–1291, doi:10.1029/96TC01791.
- Hossack, J. R., and Cooper, M. A. (1986), Collision tectonics in the Scandinavian Caledonides, in *Collision Tectonics*, edited by M. P. Coward, and A. C. Ries, *Geol. Soc. Spec. Publ.*, **19**, 287–304, doi:10.1144/gsl.sp.1986.019.01.16.
- Hurtado, J. M. (2002), Tectonic Evolution of the Thakkahola Graben and Dhaulagiri Himalaya, Central Nepal PhD thesis, 462 pp., Massachusetts Institute of Technology.
- Hurtado, J. M., K. V. Hodges, and K. X. Whipple (2001), Neotectonics of the Thakkhola graben and implications for recent activity on the South Tibetan fault system in the central Nepal Himalaya, *Geol. Soc. Am. Bull.*, **113**(2), 222–240.
- Hurtado, J. M., N. Chatterjee, J. Ramezani, K. V. Hodges, and S. A. Bowring (2007), Electron microprobe chemical dating of uraninite as a reconnaissance tool for leucogranite geochronology. [Available at <http://hdl.handle.net/10101/npre.2007.655.1>]
- Iaccarino, S., C. Montomoli, R. Carosi, H. J. Massonne, A. Langone, and D. Visonà (2015), Pressure-temperature-time-deformation path of kyanite-bearing migmatitic paragneiss in the Kali Gandaki valley (Central Nepal): Investigation of Late Eocene-Early Oligocene melting processes, *Lithos*, **231**, 103–121, doi:10.1016/j.lithos.2015.06.005.
- Iaffaldano, G., T. Bodin, and M. Sambridge (2013), Slow-downs and speed-ups of India-Eurasia convergence since: Data-noise, uncertainties and dynamic implications, *Earth Planet. Sci. Lett.*, **367**, 146–156, doi:10.1016/j.epsl.2013.02.014.
- Jamieson, R. A., and C. Beaumont (2013), On the origin of orogens, *Geol. Soc. Am. Bull.*, **125**, 1671–1702, doi:10.1130/b30855.1.
- Janák, F. (1965), Determination of anisotropy of magnetic susceptibility of rocks, *Stud. Geophys. Geod.*, **9**, 290–301.
- Jeřábek, P., H. Stünitz, R. Heilbronner, O. Lexa, and K. Schulmann (2007), Microstructural-deformation record of an orogen-parallel extension in the Vepor Unit, West Carpathians, *J. Struct. Geol.*, **29**, 1722–1743, doi:10.1016/j.jsg.2007.09.002.

- Jelinek, V. (1978), Statistical processing of anisotropy of magnetic susceptibility measured on groups of specimens, *Stud. Geophys. Geod.*, 22(1), 50–62.
- Jelinek, V. (1981), Characterization of the magnetic fabric of rocks, *Tectonophysics*, 79, T63–T67.
- Jessup, M. J., and J. M. Cottle (2010), Progression from south-directed extrusion to orogen-parallel extension in the southern margin of the Tibetan Plateau, Mount Everest Region, Tibet, *J. Geol.*, 118, 467–486, doi:10.1086/655011.
- Jessup, M. J., D. L. Newell, J. M. Cottle, A. L. Berger, and J. A. Spotila (2008), Orogen-parallel extension and exhumation enhanced by denudation in the trans-Himalayan Arun River gorge, Ama Drime Massif, Tibet-Nepal, *Geology*, 36, 587–590, doi:10.1130/G24722a.1.
- Knipe, R. J., and R. D. Law (1987), The influence of crystallographic orientation and grain boundary migration on microstructural and textural evolution in an S-C mylonite, *Tectonophysics*, 135, 155–169, doi:10.1016/0040-1951(87)90158-2.
- Kruckenberg, S. C., E. C. Ferré, C. Teyssier, O. Vanderhaeghe, D. L. Whitney, N. C. A. Seaton, and J. A. Skord (2010), Viscoplastic flow in migmatites deduced from fabric anisotropy: An example from the Naxos dome, Greece, *J. Geophys. Res.*, 115, B09401, doi:10.1029/2009JB007012.
- Kruckenberg, S. C., O. Vanderhaeghe, E. C. Ferré, C. Teyssier, and D. L. Whitney (2011), Flow of partially molten crust and the internal dynamics of a migmatite dome, Naxos, Greece, *Tectonics*, 30, TC3001, doi:10.1029/2010TC002751.
- Langille, J. M., M. J. Jessup, J. Cottle, and T. Ahmad (2014), Kinematic and thermal studies of the Leo Pargil Dome: Implications for synconvergent extension in the NW Indian Himalaya, *Tectonics*, 33, 1766–1786, doi:10.1002/2014TC003593.
- Larson, K. P., and J. M. Cottle (2015), Initiation of crustal shortening in the Himalaya, *Terra Nova*, 27, 169–174, doi:10.1111/ter.12145.
- Larson, K. P., and L. Godin (2009), Kinematics of the Greater Himalayan sequence, Dhaulagiri Himal: Implications for the structural framework of central Nepal, *J. Geol. Soc. London*, 166, 25–43, doi:10.1144/0016-76492007-180.
- Larson, K. P., L. Godin, and R. A. Price (2010), Relationships between displacement and distortion in orogens: Linking the Himalayan foreland and hinterland in central Nepal, *Geol. Soc. Am. Bull.*, 122, 1116–1134, doi:10.1130/B30073.1.
- Larson, K. P., T. K. Ambrose, A. A. G. Webb, J. M. Cottle, and S. Shrestha (2015), Reconciling Himalayan midcrustal discontinuities: The Main Central thrust system, *Earth Planet. Sci. Lett.*, 429, 139–146.
- Law, R. D. (2010), Moine thrust zone mylonites at the Stack of Glencoul: II. Results of vorticity analyses and their tectonic significance, in *Continental Tectonics and Mountain Building—The Legacy of Peach and Horne*, edited by R. D. Law et al., *Geol. Soc. Spec. Publ.*, 335, 579–602, doi:10.1144/SP335.24.
- Law, R. D., D. W. Stahr, M. K. Francis, K. T. Ashley, B. Grasemann, and T. Ahmad (2013), Deformation temperatures and flow vorticities near the base of the Greater Himalayan Series, Sutlej Valley and Shimla klippe, NW India, *J. Struct. Geol.*, 54, 21–53, doi:10.1016/j.jsg.2013.05.009.
- Le Fort, P. (1981), Manaslu leucogranite: A collision signature of the Himalaya—A model for its genesis and emplacement, *J. Geophys. Res.*, 86, 10,545–10,568, doi:10.1029/JB086iB11p10545.
- Le Fort, P., A. Pêcher, and B. N. Upreti (1987), A section through the Tibetan Slab in central Nepal (Kali Gandaki valley): Mineral chemistry and thermobarometry of the Main Central Thrust zone, in *Orogenic Evolution of Southern Asia (From Turkey to Indonesia)*, Nancy, edited by P. Le Fort, M. Colchen, and C. Montenat, pp. 211–228, Sciences de la Terre, France.
- Lloyd, G. E. (1987), Atomic number and crystallographic contrast images with the SEM: A review of backscattered electron techniques, *Mineral. Mag.*, 51, 3–19.
- Martín-Hernández, F., and E. C. Ferré (2007), Separation of paramagnetic and ferrimagnetic anisotropies: A review, *J. Geophys. Res.*, 112, B03105, doi:10.1029/2006JB004340.
- Martín-Hernández, F., and A. M. Hirt (2003), The anisotropy of magnetic susceptibility in biotite, muscovite and chlorite single crystals, *Tectonophysics*, 367, 13–28, doi:10.1016/S0040-1951(03)00127-6.
- McCaffrey, R., and J. Nabelek (1998), Role of oblique convergence in the active deformation of the Himalayas and southern Tibet Plateau, *Geology*, 26, 691–694.
- McDermott, J. A., K. V. Hodges, K. X. Whipple, M. C. V. Soest, and J. M. Hurtado (2015), Evidence for Pleistocene low-angle normal faulting in the Annapurna-Dhaulagiri Region, Nepal, *J. Geol.*, 123, 133–151, doi:10.1086/681219.
- Merle, O. (1989), Strain models within spreading nappes, *Tectonophysics*, 165, 57–71, doi:10.1016/0040-1951(89)90035-8.
- Montomoli, C., R. Carosi, and S. Iaccarino (2015), Tectonometamorphic discontinuities in the Greater Himalayan Sequence: A local or a regional feature? in *Tectonics of the Himalaya*, edited by S. Mukherjee et al., *Geol. Soc. Spec. Publ.*, 412, 25–41.
- Molnar, P., and J. M. Stock (2009), Slowing of India's convergence with Eurasia since 20 Ma and its implications for Tibetan mantle dynamics, *Tectonics*, 28, TC3001, doi:10.1029/2008TC002271.
- Mottram, C. M., R. R. Parrish, D. Regis, C. J. Warren, T. W. Argles, N. B. W. Harris, and N. M. W. Roberts (2015), Using U-Th-Pb petrochronology to determine rates of ductile thrusting: Time windows into the Main Central Thrust, Sikkim Himalaya, *Tectonics*, 34, 1355–1374, doi:10.1002/2014TC003743.
- Mukherjee, S. (2013), Higher Himalaya in the Bhagirathi section (NW Himalaya, India): Its structures, backthrusts and extrusion mechanism by both channel flow and critical taper mechanisms, *Int. J. Earth Sci.*, 102, 1851–1870, doi:10.1007/s00531-012-0861-5.
- Mukherjee, S. (2015), A review on out-of-sequence deformation in the Himalaya, in *Tectonics of the Himalaya*, edited by S. Mukherjee et al., *Geol. Soc. Spec. Publ.*, 412, 67–109, doi:10.1144/sp412.13.
- Murphy, M., M. Taylor, J. Gosse, C. Silver, D. Whipp, and C. Beaumont (2014), Limit of strain partitioning in the Himalaya marked by large earthquakes in western Nepal, *Nat. Geosci.*, 7, 38–42.
- Murphy, M. A., and P. Copeland (2005), Transensional deformation in the central Himalaya and its role in accommodating growth of the Himalayan orogen, *Tectonics*, 24, TC4012, doi:10.1029/2004TC001659.
- Muxworthy, A., D. Heslop, and W. Williams (2004), Influence of magnetostatic interactions on first-order-reversal-curve (FORC) diagrams: A micromagnetic approach, *Geophys. J. Int.*, 158, 888–897, doi:10.1111/j.1365-246X.2004.02358.x.
- Nagy, C., L. Godin, B. Antolin, J. Cottle, and D. Archibald (2015), Mid-Miocene initiation of orogen-parallel extension, NW Nepal Himalaya, *Lithosphere*, doi:10.1130/L425.1.
- Najman, Y., et al. (2010), Timing of India-Asia collision: Geological, biostratigraphic, and palaeomagnetic constraints, *J. Geophys. Res.*, 115, B12416, doi:10.1029/2010JB007673.
- Nazarchuk, J. H. (1993), Structure and geochronology of the Greater Himalaya, Kali Gandaki region, west-central Nepal MS thesis, Carleton Univ., Ottawa, Ontario.
- Parsons, A. J., R. D. Law, G. E. Lloyd, R. J. Phillips, and M. P. Searle (2016a), Thermo-kinematic evolution of the Annapurna-Dhaulagiri Himalaya, central Nepal: The Composite Orogenic System, *Geochem. Geophys. Geosyst.*, 17, 1511–1539, doi:10.1002/2015GC006184.
- Parsons, A. J., R. J. Phillips, G. E. Lloyd, R. D. Law, M. P. Searle, and R. D. Walshaw (2016b), Mid-crustal deformation of the Annapurna-Dhaulagiri Himalaya, central Nepal: An atypical example of channel flow during the Himalayan orogeny, *Geosphere*, 12, 1–31, doi:10.1130/GES01246.1.
- Parsons, A. J., R. D. Law, M. P. Searle, R. J. Phillips, and G. E. Lloyd (2016c), Geology of the Dhaulagiri-Annapurna-Manaslu Himalaya, Western Region, Nepal. 1:200,000, *J. Maps*, 12, 100–110, doi:10.1080/17445647.2014.984784.

- Pêcher, A. (1991), The contact between the Higher Himalaya Crystallines and the Tibetan Sedimentary Series: Miocene large-scale dextral shearing, *Tectonics*, *10*, 587–598, doi:10.1029/90TC02655.
- Pêcher, A., J.-L. Bouchez, and P. Le Fort (1991), Miocene dextral shearing between Himalaya and Tibet, *Geology*, *19*, 683–685, doi:10.1130/0091-7613(1991)019<0683:mdsbha>2.3.co;2.
- Pike, C. R., A. P. Roberts, and K. L. Verosub (1999), Characterizing interactions in fine magnetic particle systems using first order reversal curves, *J. Appl. Phys.*, *85*, 6660–6667, doi:10.1063/1.370176.
- Pokorný, J., P. Suza, and F. Hrouda (2004), Anisotropy of magnetic susceptibility of rocks measured in variable weak magnetic fields using the KLY-4S Kappabridge, in *Magnetic Fabric: Methods and Application*, edited by F. Martín-Hernández et al., *Geol. Soc. Spec. Publ.*, *238*, 69–76.
- Potter, D. K., and A. Stephenson (1988), Single-domain particles in rocks and magnetic fabric analysis, *Geophys. Res. Lett.*, *15*, 1097–1100, doi:10.1029/GL015i010p01097.
- Prior, D. J., et al. (1999), The application of electron backscatter diffraction and orientation contrast imaging in the SEM to textural problems in rocks, *Am. Mineral.*, *84*, 1741–1759.
- Ramsay, J., and M. Huber (1983), *The Techniques of Modern Structural Analysis, Strain Anal.*, vol. 1, pp. 307, Academic Press, London.
- Ratschbacher, L., W. Frisch, H.-G. Linzer, and O. Merle (1991), Lateral extrusion in the eastern Alps. Part 2: Structural analysis, *Tectonics*, *10*, 257–271, doi:10.1029/90TC02623.
- Ring, U. (1992), The kinematic history of the Pennine Nappes east of the Lepontine Dome: Implications for the tectonic evolution of the Central Alps, *Tectonics*, *11*, 1139–1158, doi:10.1029/92TC00616.
- Roberts, A. P., C. R. Pike, and K. L. Verosub (2000), First-order reversal curve diagrams: A new tool for characterizing the magnetic properties of natural samples, *J. Geophys. Res.*, *105*(B12), 28,461–28,475, doi:10.1029/2000JB900326.
- Roberts, A. P., Q. S. Liu, C. J. Rowan, L. Chang, C. Carvallo, J. Torrent, and C. S. Horng (2006), Characterization of hematite ( $\alpha$ -Fe<sub>2</sub>O<sub>3</sub>), goethite ( $\alpha$ -FeOOH), greigite (Fe<sub>3</sub>S<sub>4</sub>), and pyrrhotite (Fe<sub>7</sub>S<sub>8</sub>) using first-order reversal curve diagrams, *J. Geophys. Res.*, *111*, B12S35, doi:10.1029/2006JB004715.
- Rochette, P., B. Scaillet, S. Guillot, P. Le Fort, and A. Pêcher (1994), Magnetic properties of the High Himalayan leucogranites: Structural implications, *Earth Planet. Sci. Lett.*, *126*, 217–234, doi:10.1016/0012-821X(94)90108-2.
- Royden, L. H., B. C. Burchfiel, and R. D. Van Der Hilst (2008), The geological evolution of the Tibetan Plateau, *Science*, *321*(5892), 1054–1058, doi:10.1126/science.1155371.
- Scaillet, B., A. Pêcher, P. Rochette, and M. Champenois (1995), The Gangotri granite (Garhwal Himalaya): Laccolithic emplacement in an extending collisional belt, *J. Geophys. Res.*, *100*(B1), 585–607, doi:10.1029/94JB01664.
- Schmid, S. M., T. Berza, V. Diaconescu, N. Froitzheim, and B. Fügenschuh (1998), Orogen-parallel extension in the Southern Carpathians, *Tectonophysics*, *297*, 209–228, doi:10.1016/S0040-1951(98)00169-3.
- Searle, M. P. (2010), Low-angle normal faults in the compressional Himalayan orogen: Evidence from the Annapurna-Dhaulagiri Himalaya, Nepal, *Geosphere*, *6*, 296–315, doi:10.1130/Ges00549.1.
- Searle, M. P. (2015), Mountain building, tectonic evolution, rheology, and crustal flow in the Himalaya, Karakoram, and Tibet, in *Treatise on Geophysics*, vol. 6, 2nd ed., edited by G. Schubert, pp. 469–511, Elsevier, Oxford.
- Searle, M. P., R. D. Law, L. Godin, K. P. Larson, M. J. Streule, J. M. Cottle, and M. J. Jessup (2008), Defining the Himalayan Main Central Thrust in Nepal, *J. Geol. Soc. London*, *165*, 523–534.
- Searle, M. P., R. D. Law, and M. J. Jessup (2006), Crustal structure, restoration and evolution of the Greater Himalaya in Nepal-South Tibet: Implications for channel flow and ductile extrusion of the middle crust, in *Channel Flow, Ductile Extrusion and Exhumation in Continental Collision Zones*, edited by R. D. Law, M. P. Searle, and L. Godin, *Geol. Soc. Spec. Publ.*, *268*, 355–378.
- Searle, M. P., J. R. Elliott, R. J. Phillips, and S. L. Chung (2011), Crustal-lithospheric structure and continental extrusion of Tibet, *J. Geol. Soc.*, *168*, 633–672, doi:10.1144/0016-76492010-139.
- Sherrington, H. F., G. Zandt, and A. Frederiksen (2004), Crustal fabric in the Tibetan Plateau based on waveform inversions for seismic anisotropy parameters, *J. Geophys. Res.*, *109*, B02312, doi:10.1029/2002JB002345.
- Sidman, D., E. C. Ferré, C. Teysier, and M. Jackson (2005), Magnetic fabric and microstructure of a mylonite: Example from the Bitterroot shear zone, western Montana, in *High-Strain Zones: Structure and Physical Properties*, edited by D. Bruhn and L. Burlini, *Geol. Soc. Spec. Publ.*, *245*, 143–163.
- Silver, C. R. P., M. A. Murphy, M. H. Taylor, J. Gosse, and T. Baltz (2015), Neotectonics of the Western Nepal Fault System: Implications for Himalayan strain partitioning, *Tectonics*, *34*, 2494–2513, doi:10.1002/2014TC003730.
- Stephenson, A. (1994), Distribution anisotropy: Two simple models for magnetic lineation and foliation, *Phys. Earth Planet. Inter.*, *82*, 49–53, doi:10.1016/0031-9201(94)90101-5.
- Styron, R. H., M. H. Taylor, and M. A. Murphy (2011), Oblique convergence, arc-parallel extension, and the role of strike-slip faulting in the High Himalaya, *Geosphere*, *7*, 582–596.
- Sylvester, A. G., and D. R. Janecky (1988), Structure and petrofabrics of quartzite and elongate pebbles at Sandviksfjell, Bergen, Norway, *Nor. Geol. Tidsskr.*, *68*, 31–50.
- Tarling, D. H., and F. Hrouda (1993), *The Magnetic Anisotropy of Rocks*, 217 pp., Chapman and Hall, London.
- Tauxe, L. (2002), *Paleomagnetic Principles and Practice*, 311 pp., Springer, Dordrecht.
- Tauxe, L., T. A. T. Mullender, and T. Pick (1996), Potbellies, wasp-waists, and superparamagnetism in magnetic hysteresis, *J. Geophys. Res.*, *101*(B1), 571–583, doi:10.1029/95JB03041.
- Tripathy, N. R. (2009), Degree of magnetic anisotropy as a strain-intensity gauge in a saturated finite-strain zone, *J. Geol. Soc.*, *166*, 9–12, doi:10.1144/0016-76492008-078.
- Vannay, J. C., and K. V. Hodges (1996), Tectonometamorphic evolution of the Himalayan metamorphic core between the Annapurna and Dhaulagiri, central Nepal, *J. Metamorph. Geol.*, *14*, 635–656.
- Vannay, J.-C., and A. Steck (1995), Tectonic evolution of the High Himalaya in Upper Lahul (NW Himalaya, India), *Tectonics*, *14*, 253–263, doi:10.1029/94TC02455.
- Viola, G., and Henderson, I. C. (2010), Inclined transpression at the toe of an arcuate thrust: An example from the Precambrian “Mylonite Zone” of the Sveconorwegian orogen, in *Continental Tectonics and Mountain Building—The Legacy of Peach and Horne*, edited by R. D. Law et al., *Geol. Soc. Spec. Publ.*, *335*, 715–737, doi:10.1144/SP335.29.
- Wallis, D., A. J. Parsons, R. J. Phillips, M. P. Searle, and E. C. Ferré (2014a), Comment on “Interplay of deformation and magmatism in the Pangong Transpression Zone, Eastern Ladakh, India: Implications for remobilization of the trans-Himalayan magmatic arc and initiation of the Karakoram Fault” by K. Sen, B. K. Mukherjee & A. S. Collins, *Journal of Structural Geology*, *62*, (2014) 13–24, *J. Struct. Geol.*, *65*, 117–119.

- Wallis, D., R. J. Phillips, and G. E. Lloyd (2014b), Evolution of the Eastern Karakoram Metamorphic Complex, Ladakh, NW India, and its relationship to magmatism and regional tectonics, *Tectonophysics*, 626, 41–52, doi:10.1016/j.tecto.2014.03.023.
- Wallis, D., G. E. Lloyd, R. J. Phillips, A. J. Parsons, and R. D. Walshaw (2015), Low effective fault strength due to frictional-viscous flow in phyllonites, Karakoram Fault Zone, NW India, *J. Struct. Geol.*, 77, 45–61, doi:10.1016/j.jsg.2015.05.010.
- Westaway, R. (1995), Crustal volume balance during the India-Eurasia collision and altitude of the Tibetan Plateau: A working hypothesis, *J. Geophys. Res.*, 100, 15,173–15,192, doi:10.1029/95JB01310.
- Whipp, D. M., C. Beaumont, and J. Braun (2014), Feeding the “aneurysm”: Orogen-parallel mass transport into Nanga Parbat and the western Himalayan syntaxis, *J. Geophys. Res. Solid Earth*, 119, 5077–5096, doi:10.1002/2013JB010929.
- Williams, J. R., and J. P. Platt (2013), Crustal-scale ductile thinning of the Alboran Domain—Structural and petrological analysis from the Alpujarride Complex, Betic Cordillera, S. Spain GSA Annual Meeting, Denver, Colo., 45, 601.
- Woodcock, N. H. (1977), Specification of fabric shapes using an eigenvalue method, *Geol. Soc. Am. Bull.*, 88, 1231–1236, doi:10.1130/0016-7606(1977)88<1231:sofsua>2.0.co;2.
- Xu, Z., Q. Wang, A. Pêcher, F. Liang, X. Qi, Z. Cai, H. Li, L. Zeng, and H. Cao (2013), Orogen-parallel ductile extension and extrusion of the Greater Himalaya in the late Oligocene and Miocene, *Tectonics*, 32, 191–215, doi:10.1002/tect.20021.